Applied Catalysis B: Environmental 96 (2010) 276–289

Contents lists available at ScienceDirect

Applied Catalysis B: Environmental

journal homepage: www.elsevier.com/locate/apcatb

Low-temperature purification of gas streams from phenol by steam reforming over novel supported-Rh catalysts

Domna A. Constantinou, Angelos M. Efstathiou *

Heterogeneous Catalysis Laboratory, Department of Chemistry, University of Cyprus, P.O. Box 20537, CY 1678 Nicosia, Cyprus

ARTICLE INFO

Article history:
Received 17 October 2009
Received in revised form 3 February 2010
Accepted 5 February 2010
Available online 11 February 2010

Keywords:
Phenol steam reforming
Hydrogen production
Supported-Rh catalysts
CO_2–TPD
CO–TPD
CO–DRIFTS
WGS–DRIFTS

ABSTRACT

The purification of gas streams from phenol at low-temperatures (350–550 °C) was investigated by its reaction with steam over novel catalytic systems, namely 0.5 wt% Rh supported on $Ce_{0.15}Zr_{0.85}O_2$, $Ce_{0.15}Zr_{0.83}Mg_{0.02}O_2$ and $Ce_{0.14}Zr_{0.81}Mg_{0.05}O_2$ mixed metal oxides. It was found that the rate of reforming reaction was largely influenced by the support chemical composition, where catalytic activity and selectivity towards H_2 formation were increased with increasing support Mg content (0–5 atom%). The 0.5 wt% $Rh/Ce_{0.14}Zr_{0.81}Mg_{0.05}O_2$ catalyst showed the best activity in terms of phenol conversion and H_2-yield, and the lowest CO/CO_2 product ratio in the 350–550 °C range. In particular, at 450 °C a phenol conversion of about 80% and a H_2-yield of about 85% were obtained for a feed containing 0.6 vol.% phenol and 40 vol.% H_2O at a gas hourly space velocity of 54,000 h^{-1}. The latter catalyst composition exhibited significantly better catalytic performance in the 350–450 °C range when compared to a commercial Ni-based catalyst used for tar steam reforming. In particular, at 450 °C the H_2-yield was increased by 75% and the CO/CO_2 product ratio decreased by a factor of eight compared to the commercial Ni-based catalyst. It was found that the catalytic behaviour of 0.5 wt% $Rh/Ce_{0.14}Zr_{0.81}Mg_{0.05}O_2$ correlates with the presence of a larger concentration of basic sites, a larger concentration of labile oxygen species, and of very small mean Rh particle size (~1.3 nm) compared to the other supported-Rh catalysts investigated. The significantly lower CO/CO_2 product ratio obtained in the $Rh/Ce_{0.14}Zr_{0.81}Mg_{0.05}O_2$ compared to the other supported-Rh catalysts was related to the presence of a large surface concentration of Rh^{n+} cationic sites which may promote the water–gas shift (WGS) reaction. The activity towards the WGS reaction was found to be promoted by the presence of Mg^{2+} in the support composition. *In situ* DRIFTS–WGS reaction studies revealed that the kinds and surface concentration of formate species formed, likely active reaction intermediates in the WGS reaction, depend on the chemical support composition. The $Ce_{0.14}Zr_{0.81}Mg_{0.05}O_2$ support when used to deposit the same amount of Rh metal (0.5 wt%) resulted in a larger concentration of formate species than the $Ce_{0.15}Zr_{0.85}O_2$ support. This result could partly explain the significantly larger phenol steam reforming activity towards H_2 and CO_2 observed on the $Rh/Ce_{0.14}Zr_{0.81}Mg_{0.05}O_2$ than $Rh/Ce_{0.15}Zr_{0.85}O_2$ catalyst.

1. Introduction

The use of fossil fuels as the main energy source has caused serious environmental problems demanding the utmost need for clean and environmentally friendly fuels [1]. Hydrogen has been identified as a suitable and very promising energy carrier for this purpose [2]. In order to support sustainable hydrogen economy, it is important to produce hydrogen in a clean and sustainable way. The design and development of hydrogen production technologies from biomass or waste-biomass fuels is highly considered as a promising approach due to its large availability and CO_2-neutral nature [3,4].

Among the thermo-chemical biomass conversion techniques [5], catalytic steam gasification is a vital one that converts biomass into "biosyngas" (mixture of H_2, CO, and CO_2) [6–10]. The resulting biomass-derived raw "biosyngas" contains undesirable components, such as tar, hydrogen sulphide, hydrocarbons, ammonia, and hydrogen chloride [6,9]. It is considered that formation of tar is a significant technical impediment to the use of biomass or waste-biomass as fuels in commercial gasification systems [6,9,10]. Tar is defined as the condensable fraction of organics produced under thermal or partial-oxidation of any organic material, largely consisting of aromatic compounds [9]. The presence of tars in "biosyngas" is considered as equivalent to a major economic penalty in biomass gasification [11]. Tar aerosols and deposits

* Corresponding author. Tel.: +357 22 892776; fax: +357 22 892801.
E-mail address: efstath@ucy.ac.cy (A.M. Efstathiou).

0926-3373/$ – see front matter © 2010 Elsevier B.V. All rights reserved.
doi:10.1016/j.apcatb.2010.02.007

result to an increased necessity for a downstream gas purification processing due to the several problems associated with condensation, which may cause clog of fuel lines, block of gas engines and turbines, catalyst poisoning in the further processing of "biosyngas", and increasing maintenance costs [12]. The addition of steam and the use of gasification temperatures lower than 800 °C were found to form oxygen-containing compounds such as phenol, cresol and benzofuran [13]. Phenol was further identified as the constituent molecule of tar formed following wood-biomass gasification by steam in a fluidized bed reactor in the 600–700 °C range at 1 bar [14].

Several measures for tar removal have been investigated and these can be divided in *primary*, measures inside the gasifier, or *secondary*, measures downstream of the gasifier [11]. Although measures inside the gasifier may be considered more ideal, they have not yet resulted in satisfactory solutions [11] and complete removal of tars is not feasible without applying secondary measures. The latter includes: (a) thermal cracking [15], (b) wet scrubbing [16], and (c) catalytic reforming [9,17,18]. The latter was reported as the best way to destroy tar components and increase product gas heating value and overall biomass utilisation efficiency [9,18].

Several catalysts promoted with chemical additives have been used towards purification of biomass-derived "biosyngas" from tars, where Ni/γ-Al_2O_3 is one of the most extensively used commercial catalytic systems. In general, supported-Ni catalysts demonstrate high tar conversion with simultaneous NH_3 reduction [19]. The major problem with Ni-based catalysts is their fast deactivation caused by carbon deposition and their poisoning due to the presence of H_2S. Another limitation of these catalysts is their low attrition resistance preventing their applications in fluidized-bed reactors. On the other hand, supported-Rh catalysts were reported to exhibit similar catalytic activity and much lower surface carbon deposition [20,21]. The addition of basic metal oxides on the support was shown to retard coke deposition [22]. Solids exhibiting significant concentration of highly mobile oxygen species (e.g., $Ce_xZr_{1-x}O_2$) were also proposed to be suitable for coke suppression [21].

Rh/CeO_2 and Rh/CeO_2–SiO_2 catalysts were investigated towards steam reforming of cellulose and biomass gasification in the 500–750 °C range, where coking was significantly reduced compared to the Ni-based catalysts investigated [23–28]. The phenol steam reforming leading to H_2, CO and CO_2 formation over supported-Rh catalysts in the 575–730 °C range was first reported by Polychronopoulou et al. [29,30]. Supported-Rh catalysts could be considered as potential industrial catalytic systems for "biosyngas" purification from tars in fixed-bed reactor applications, where low Rh loadings (<1 wt%) and low reaction temperatures ($T < 500$ °C) could reduce significantly operational costs.

The present work aimed to investigate for the *first time* the steam reforming of phenol in the 350–550 °C low-temperature range in a fixed-bed micro-reactor over Ce–Zr–Mg–O mixed metal–oxide supported-Rh catalysts as a means to provide a very clean product gas derived from biomass gasification by steam technologies. BET, X-ray diffraction, H_2, CO and CO_2 temperature-programmed desorption (TPD), H_2 temperature-programmed reduction (H_2-TPR), and *in situ* Diffuse Reflectance Infrared Fourier Transform Spectroscopy (DRIFTS)–CO chemisorption studies were conducted in an effort to gather fundamental knowledge in order to facilitate the correct interpretation of the catalytic behaviour of the former solids. The catalytic behaviour of supported-Rh solids was compared to a commercial Ni-based catalyst at the same experimental conditions. The water–gas shift (WGS) reaction was also studied over the present Ce–Zr–Mg–O mixed metal–oxide supported-Rh catalysts in terms of activity and reaction intermediates (use of *in situ* DRIFTS). These results were used to better explain the phenol steam reforming catalytic activity of the same solids.

2. Experimental

2.1. Catalyst preparation

Commercial $Ce_{0.15}Zr_{0.85}O_2$, $Ce_{0.15}Zr_{0.83}Mg_{0.02}O_2$, and $Ce_{0.14}Zr_{0.81}Mg_{0.05}O_2$ (atom% composition) mixed metal oxides (MEL Chemicals, UK) were used as supports of Rh metal. These metal oxides were synthesised after using the same commercial proprietary co-precipitation method. They were calcined in air at 750 °C for 5 h before Rh deposition. Each support was impregnated with an appropriate amount of $Rh(NO_3)_3$ (Aldrich) in distilled de-ionised water so as to yield the desirable metal loading (0.5 wt%) under constant solution pH, which was adjusted to 9.5 by dropwise addition of ammonia solution at 60 °C. The resulting solid was then dried overnight at 120 °C and kept in storage for further use.

2.2. Catalyst characterization

2.2.1. SSA and Rh dispersion measurements

The BET method (adsorption of N_2 at 77 K) was applied in a Micromeritics Gemini III Surface Area and Pore size Analyzer in order to determine the specific surface area (SSA, $m^2\,g^{-1}$), the specific pore volume ($cm^3\,g^{-1}$), and the average pore diameter (nm) of the calcined (use of air at 750 °C for 5 h) $Ce_{0.15}Zr_{0.85}O_2$, $Ce_{0.15}Zr_{0.83}Mg_{0.02}O_2$ and $Ce_{0.14}Zr_{0.81}Mg_{0.05}O_2$ solids. Each measurement was taken after the sample was outgassed *in situ* at 200 °C under vacuum ($P \approx 1.3 \times 10^{-3}$) for 2 h.

The Rh dispersion of the catalysts was determined by H_2 selective chemisorption followed by TPD in He flow in a specially designed gas flow system as previously described [31]. A 0.5-g catalyst sample and a 30 N mL/min total flow rate were used. The fresh catalyst sample was first calcined in 20% O_2/He gas mixture at 600 °C for 2 h, and then reduced in pure H_2 (1 bar) at 200 °C for 2 h. The catalyst was then purged in He at 500 °C until no H_2 evolution was observed, and then cooled quickly in He flow to 100 °C. A 1 vol.% H_2/He gas mixture was then passed over the catalyst at 100 °C for 30 min. After this adsorption step the catalyst was cooled quickly in 1 vol.% H_2/He to room temperature and kept for 15 min. A switch to He flow was then made for 15 min, and the temperature of the catalyst was increased from room temperature to 700 °C to carry out a temperature-programmed desorption (TPD) experiment.

2.2.2. X-ray diffraction studies

The crystal structures of the calcined in air (750 °C, 5 h) commercial mixed metal oxides ($Ce_{0.15}Zr_{0.85}O_2$, $Ce_{0.15}Zr_{0.83}Mg_{0.02}O_2$, and $Ce_{0.14}Zr_{0.81}Mg_{0.05}O_2$) were checked by powder X-ray diffraction (XRD) (Shimadzu 6000, Cu-Kα radiation (λ = 1.5418 Å)). The primary mean crystallite size (d_c, nm) was determined using the Scherrer equation [32]. Each sample was crushed and sieved to lower than 200 mesh size before XRD measurements were conducted. Diffractograms were recorded in the 2θ range between 10 and 80° with a step scan of 2° min^{-1}.

2.2.3. H_2 temperature-programmed reduction (H_2-TPR) studies

H_2 temperature-programmed reduction (H_2-TPR) experiments were conducted in a specially designed gas flow-system previously described [31] over the air-calcined commercial mixed metal oxides and the supported-Rh catalysts. All solids were first pre-treated in 20% O_2/He at 600 °C for 2 h, purged in He, and then cooled to room temperature. A 2 vol.% H_2/He gas mixture was then passed to the reactor and the temperature of the solid was increased to 800 °C at the rate of 30 °C/min. The mass numbers (m/z) 2, 18, 32 were used for H_2, H_2O and O_2, respectively. Based on material balance, the rate of hydrogen consumption (μmol H_2/(g s)) versus temperature was estimated.

2.2.4. CO_2 temperature-programmed desorption (CO_2–TPD) studies

Temperature-programmed desorption of CO_2 experiments were conducted in a specially designed gas flow-system described elsewhere [31]. The commercial mixed metal oxides (0.5 g) were first calcined in 20% O_2/He at 600 °C for 2 h, whereas the supported-Rh catalysts (0.5 g) were first reduced in pure H_2 at a given T (T = 300, 500, and 700 °C) for 2 h following pre-treatment in 20% O_2/He at 600 °C for 2 h. CO_2–TPDs at different reduction temperatures of the solid were performed in order to investigate the effect of oxygen vacant sites formed on the support after H_2 reduction on the CO_2 chemisorption and desorption behavior. After the above treatment steps the feed was changed to He for 15 min and the reactor was cooled to room temperature. The feed was subsequently switched to 3 vol.% CO_2/He gas mixture for 30 min and then to He (30 N mL/min) for 15 min until no signal of CO_2 was detected in the mass spectrometer (Omnistar, Balzers), which was equipped with a fast response inlet capillary/leak valve (SVI050, Balzers) and data acquisition systems. The temperature of the solid was then increased from room temperature to 800 °C at the rate of 30 °C/min (TPD run). Calibration of the CO_2 signal (m/z = 44) of the mass spectrometer was made based on a 1 vol.% CO_2/He calibration gas mixture.

2.2.5. CO temperature-programmed desorption (CO–TPD) studies

CO–TPD experiments were performed following chemisorption of CO at 25 °C over the supported-Rh catalysts (0.5 g) under 30 N mL/min He flow rate and 30 °C/min heating rate of the solid catalyst. The catalyst was first pre-treated in 20% O_2/He at 600 °C for 2 h and then reduced in pure H_2 (1 bar) at 200 °C for 2 h. The catalyst was then purged in He flow at 500 °C until no H_2 evolution was observed and cooled quickly to room temperature. A 2 vol.% CO/He gas mixture was then switched to the reactor for 30 min followed by a switch to He flow and increase of the temperature of the solid to 700 °C (CO–TPD run). Following the CO–TPD run the feed was changed to He at 700 °C until the CO (m/z = 28) and CO_2 (m/z = 44) mass spectrometer signals reached their respective baseline value. The gas flow was then switched to 2% O_2/He and the signals of CO and CO_2 were continuously recorded by *on line* mass spectrometer. The amount of surface "carbonaceous" deposits (μmol C/g catalyst) was calculated based on the CO and CO_2 response curves calibrated against standard mixtures and the appropriate carbon mass balance for a flow-reactor.

2.2.6. Oxygen storage capacity (OSC) measurements

The oxygen storage capacity (OSC, μmol O/g_{cat}) of supported-Rh catalysts (see Section 2.1) was measured after using the pulse injection technique [33,34]. The experimental set-up has been described elsewhere [33]. The amount (μmol O/g_{cat}) of reactive oxygen species present in the solid was estimated through the amount of H_2 consumed (H_2 pulses were used) during the reduction step or the amount of O_2 consumed during the re-oxidation step by successive oxygen pulses. The latter amount of oxygen is referred to as the "oxygen storage capacity complete", OSCC. The amount of the most reactive oxygen (labile oxygen) of the catalyst is defined as the amount of oxygen species that reacted during the first H_2 pulse (50 μmol). This is called "oxygen storage capacity", OSC. The amount of catalyst sample used was 100 mg in powder form. The catalyst sample was pre-treated in 20% O_2/He gas mixture at a given temperature (T_{OSC}) for 1 h. The reactor was then flushed in He for 15 min at T_{OSC} followed by H_2/O_2 pulse(s).

2.3. Catalytic performance studies

The experimental set-up used for evaluating the catalytic performance of the mixed metal oxides and the supported-Rh catalysts towards phenol steam reforming has been described in detail elsewhere [30]. The amount of solid catalyst used in the fixed-bed micro-reactor was 0.3 g, and the total flow rate was 200 N mL/min, resulting in a GHSV of about 54,000 h^{-1}. The reaction feed stream consisted of 0.6% C_6H_5OH/40% H_2O/59.4% He, where the water and phenol compositions were similar to those encountered at the inlet (bottom) of a fluidized-bed used in wood-biomass steam gasification [14]. Initially, the catalyst sample was pre-treated in 20% O_2/He at 600 °C for 2 h and then reduced in pure H_2 (1 bar) at 200 °C for 2 h. All catalytic tests were contacted at 1 bar total pressure. The steam reforming of phenol can be described by the following reaction network [29,30,35,36]:

$$C_6H_5OH + 5H_2O \rightarrow 6CO + 8H_2 \quad (1)$$

$$CO + H_2O \leftrightarrow CO_2 + H_2 \quad (2)$$

The conversion of phenol, X_P (%) was estimated according to the following relationship:

$$X_p(\%) = \frac{F_{CO}^{out} + F_{CO2}^{out}}{6F_P^{in}} \times 100 \quad (3)$$

where F_i^{out} (i = CO, CO_2) is the molar flow rate (mols/min) of CO or CO_2 measured experimentally at the outlet of reactor, and F_p^{in} is the molar flow rate (mols/min) of phenol in the feed stream. It is important to note that only very small concentrations of benzene and methane were experimentally measured in the product gas stream, and these are not included in Eq. (3). The hydrogen yield, Y_{H2} (%) was estimated based on the following relationship:

$$Y_{H2}(\%) = \frac{y_{H2}^{out}}{y_{H2}^{max}} \times 100 \quad (4)$$

where y_{H2}^{out} is the composition (mol%) of hydrogen at the exit gas stream from the micro-reactor, and y_{H2}^{max} is the composition (mol%) of hydrogen expected when the conversions of phenol (rxn. 1) and of the WGS reaction (rxn. 2) achieve the value of 100%. The latter can be achieved at the lowest temperature studied (350 °C) under the present reaction conditions. For the present feed composition used (0.6% C_6H_5OH/40% H_2O/59.4% He), y_{H2}^{max} is estimated to be 11.76 mol% (dry-basis).

The catalytic performance of the 0.5% Rh/$Ce_{0.15}Zr_{0.85}O_2$, 0.5% Rh/$Ce_{0.15}Zr_{0.83}Mg_{0.02}O_2$, and 0.5% Rh/$Ce_{0.14}Zr_{0.81}Mg_{0.05}O_2$ solids was studied in the 350–550 °C range, while that of supports alone at 400 and 450 °C. The effect of reaction temperature and gas hourly space velocity (GHSV, h^{-1}) on phenol conversion, hydrogen product composition (dry-basis), and CO/CO_2 product ratio were investigated. The catalytic behaviour of the supported-Rh catalysts towards the water–gas shift reaction (2) was also studied using the 1 vol.% CO/40 vol.% H_2O/59 vol.% He feed composition, representative of that found at the exit of the micro-reactor under the present phenol steam reforming reaction conditions.

2.4. In situ DRIFTS studies

2.4.1. CO chemisorption

A PerkinElmer Spectrum GX II FTIR spectrometer equipped with a high-temperature/high pressure controllable DRIFTS cell (Harrick, Praying Mantis) was used for performing *in situ* DRIFTS–CO chemisorption studies over the 0.5 wt% Rh/$Ce_{0.15}Zr_{0.85}O_2$ and 0.5 wt% Rh/$Ce_{0.14}Zr_{0.81}Mg_{0.05}O_2$ solids. The catalyst sample in a very fine powder form was placed firmly into the ceramic cup of the DRIFTS cell. Chemisorption was performed using a 2 vol.% CO/He (50 N mL/min) at 25 and 400 °C. Each sample was pre-treated *in situ* in 20% O_2/Ar at 600 °C for 2 h and reduced in pure H_2 (1 bar) at 200 °C for 2 h before any FTIR spectrum was recorded. Signal averaging was set to 50 scans per spectrum at a 2 cm^{-1} spectra resolution in the 4000–400 cm^{-1} range. The DRIFTS spectra

presented here correspond only to the adsorbed phase; the spectrum of the solid itself taken in Ar flow at the desired temperature was subtracted. DRIFTS spectra when necessary were smoothed to remove high frequency noise and further analyzed using the software Spectrum for Windows. Deconvolution and curve fitting procedures of the DRIFTS spectra were performed according to reported guidelines [37] and using Gaussian peak line shapes [38].

2.4.2. Water–gas shift (WGS) reaction studies

The apparatus used to investigate the WGS reaction in the DRIFTS reactor cell regarding the nature of adsorbed reaction intermediates formed was described elsewhere [39,40]. The WGS reaction was studied at 350 and 550 °C over the 0.5 wt% Rh/$Ce_{0.15}Zr_{0.85}O_2$ and 0.5 wt% Rh/$Ce_{0.14}Zr_{0.81}Mg_{0.05}O_2$ catalysts. The reaction feed composition used was 1 vol.% CO/40 vol.% H_2O/59 vol.% He (see Section 2.3) at a total flow rate of 100 N mL/min. The spectrum of the solid catalyst taken under 40% H_2O/Ar flow (100 N mL/min) at the desired reaction temperature, following catalyst pre-treatment (calcination in 20% O_2/Ar at 600 °C for 2 h followed by reduction with pure H_2 at 200 °C for 2 h) was subtracted from the spectrum of the solid catalyst exposed to the reaction mixture.

3. Results and discussion

3.1. Catalyst characterization

3.1.1. Catalyst texture

The specific surface area (SSA, $m^2\,g^{-1}$), pore volume ($cm^3\,g^{-1}$), and the average pore diameter (nm) of the commercial mixed metal oxides $Ce_{0.15}Zr_{0.85}O_2$, $Ce_{0.15}Zr_{0.83}Mg_{0.02}O_2$ and $Ce_{0.14}Zr_{0.81}Mg_{0.05}O_2$ investigated are listed in Table 1. It is observed that $Ce_{0.14}Zr_{0.81}Mg_{0.05}O_2$ showed the highest SSA, pore volume, and average pore diameter compared to $Ce_{0.15}Zr_{0.85}O_2$ and $Ce_{0.15}Zr_{0.83}Mg_{0.02}O_2$ solids. Addition of Mg^{2+} into $Ce_{0.15}Zr_{0.85}O_2$ solid solution matrix leads gradually to the increase of SSA, and in particular of the specific pore volume and average pore diameter. An increase by approximately 7% and 30% in the SSA after adding 2 and 5 atom% Mg^{2+}, respectively, in the $Ce_{0.15}Zr_{0.85}O_2$ solid and an increase by a factor of 2.6 and 2.2, respectively in the pore volume and average pore diameter by adding 5 atom% Mg^{2+} in the $Ce_{0.15}Zr_{0.85}O_2$ solid were seen. Similar results were reported by Wang et al. [41] in an attempt to study the structure and thermal stability of Si-doped Ce–Zr–O solid solution. It is noted that all the mixed metal oxides investigated retained mesopore structure with an average pore diameter in the 8.0–18.0 nm range.

3.1.2. XRD studies

X-ray diffractograms of $Ce_{0.15}Zr_{0.85}O_2$, $Ce_{0.15}Zr_{0.83}Mg_{0.02}O_2$ and $Ce_{0.14}Zr_{0.81}Mg_{0.05}O_2$ solids were recorded after calcination in air at 750 °C for 5 h. All the XRD patterns revealed that the solids display a single crystalline phase of pseudo-cubic CeO_2–ZrO_2 solid solution [42,43]. In the case of $Ce_{0.15}Zr_{0.83}Mg_{0.02}O_2$ and $Ce_{0.14}Zr_{0.81}Mg_{0.05}O_2$ no characteristic peaks corresponding to MgO were detected. It is important to note that the diffraction peaks corresponding to $Ce_{0.15}Zr_{0.85}O_2$ were slightly shifted to higher 2θ values with increasing Mg content. The latter result indicates the shrinkage of the Ce–Zr–Mg–O lattice caused by the introduction of Mg^{2+} into the Ce–Zr–O matrix. This is consistent with the fact that the ionic radius of Mg^{2+} (0.66 Å) is smaller compared to Zr^{4+} (0.84 Å) and Ce^{4+} (0.97 Å) resulting in the reduction of the Ce–Zr–O cell parameter due to Ce^{4+} substitution for the smaller Zr^{4+} and Mg^{2+}. It was reported [44] that introduction of metal ions that have smaller ionic radius than Ce^{4+} (e.g. Zr^{4+} and Mg^{2+}) stabilise effectively the CeO_2 matrix against thermal sintering. This result was also reported by Yue et al. [45] for the Ce–Zr–M–O (M = Mg, Ca, Sr, and Ba) solids, where the introduction of M improved the thermal stability of alumina in the Ce–Zr–M–Al_2O_3 solid support.

The mean primary crystal size, d_c (nm) of the calcined $Ce_{0.15}Zr_{0.85}O_2$, $Ce_{0.15}Zr_{0.83}Mg_{0.02}O_2$ and $Ce_{0.14}Zr_{0.81}Mg_{0.05}O_2$ solids is reported in Table 1. It is seen that the mean primary crystal size is in the 7.2–12.5 nm range, leading to the conclusion that all the commercial supports were of nano-crystalline structure. Introduction of 5 atom% Mg^{2+} in the $Ce_{0.15}Zr_{0.85}O_2$ solid solution causes a decrease by 42% of the mean primary crystal size of the resulting $Ce_{0.14}Zr_{0.81}Mg_{0.05}O_2$ solid with respect to the original one.

It is also noted here that Scanning Electron Microscopy (SEM) studies performed on the $Ce_{0.14}Zr_{0.81}Mg_{0.05}O_2$ and $Ce_{0.15}Zr_{0.85}O_2$ solids provided a secondary particle size in the range of 8–20 and 8–50 μm, respectively.

3.1.3. Rhodium dispersion, D (%)

The dispersion (D, %) of Rh and its mean particle size based on spherical geometry [46] were estimated according to the H_2-TPD procedure outlined in Section 2.2.1. The Rh dispersion was found to be 25.0, 70.0, and 76.0%, and the mean Rh particle size 4.0, 1.4 and 1.3 nm, respectively, for the 0.5% Rh/$Ce_{0.15}Zr_{0.85}O_2$, 0.5% Rh/$Ce_{0.15}Zr_{0.83}Mg_{0.02}O_2$, and 0.5% Rh/$Ce_{0.14}Zr_{0.81}Mg_{0.05}O_2$ catalysts. It is seen that by increasing the amount of Mg in the support composition, Rh dispersion increases, resulting in smaller Rh particles and a higher concentration of surface metal active sites (μmol Rh_s/g).

The favouring role of the presence of Mg^{2+} in the Ce–Zr–Mg–O mixed metal–oxide support in decreasing the Rh particle size could be understood based on the excellent work of Nagai et al. [47] who studied the sintering inhibition mechanism of platinum supported on Ce–Zr–Y–O mixed metal oxides similar to the present ones. At this point it is important to emphasize that the critical step that would determine the size of a metal particle in the final supported metal catalyst is most likely to be the calcination/reduction steps. Nagai et al. [47] have considered the question "on what property of the support does the strength of Pt–oxide–support interaction depend?". Based on EXAFS studies they showed that the Pt–O–M bond (M is the cation in the support) is key to the Pt–oxide–support interaction [47]. Thus, the *electron density of oxygen in the support oxide* predominantly influences the strength of the Pt–O–M bond and thus controls the sintering of supported-Pt nanoparticles. Based on XPS results the authors nicely demonstrated that the binding energy of the O(1s) electron decreased in the order: SiO_2, Al_2O_3, ZrO_2, TiO_2, CeO_2 and Ce–Zr–Y–O, while the Pt particle size on these oxidic support materials followed exactly the opposite trend [47].

Based on the above discussion, introduction of Mg^{2+} in the Ce–Zr–O lattice has modified the electron density of oxygen in the M–O–M′ bonds (M, M′ different metal cations in the Ce–Zr–Mg–O support) resulting in stronger Rh–O–M (M′) interactions under calcination conditions. During hydrogen reduction the Rh–O–M (M′) bonds break, and Rh metal is highly dispersed on the support. The modification of the electron density of oxygen in the M–O–M′

Table 1
Textural and mean primary crystal size characteristics of commercial $Ce_{0.15}Zr_{0.85}O_2$, $Ce_{0.15}Zr_{0.83}Mg_{0.02}O_2$ and $Ce_{0.14}Zr_{0.81}Mg_{0.05}O_2$ mixed metal oxides after calcination in air at 750 °C for 5 h.

Solid	SSA ($m^2\,g^{-1}$)	Pore volume ($cm^3\,g^{-1}$)	Average pore diameter (nm)	Mean primary crystal size, d_c (nm)
$Ce_{0.15}Zr_{0.85}O_2$	42.6	0.12	8.2	12.5
$Ce_{0.15}Zr_{0.83}Mg_{0.02}O_2$	45.7	0.13	9.2	9.3
$Ce_{0.14}Zr_{0.81}Mg_{0.05}O_2$	55.5	0.31	18.2	7.2

bond of Ce–Zr–Mg–O mixed oxide was also probed in the present work through CO_2 chemisorption/TPD studies to be discussed in Section 3.1.5.

3.1.4. H_2-TPR studies

H_2-TPR measurements were carried out in order to investigate the reducibility of support alone and that after Rh deposition. Fig. 1a and b show H_2-TPR traces in terms of H_2 consumption rate (μmol H_2/g s) versus temperature obtained over the commercial mixed metal oxides (Fig. 1a) and the respective supported-Rh catalysts (Fig. 1b). Reduction of all three mixed metal oxides starts at ~400 °C (Fig. 1a) with broad reduction peaks in the 500–800 °C range. The $Ce_{0.15}Zr_{0.85}O_2$ solid solution exhibits a broad reduction peak centered at 610 °C with large and broad shoulder on its falling part. In the case of $Ce_{0.15}Zr_{0.83}Mg_{0.02}O_2$ and $Ce_{0.14}Zr_{0.81}Mg_{0.05}O_2$ solids, a single broad and larger reduction peak was detected with peak maxima at 738 and 750 °C, respectively. Moreover, it is observed that the presence of Mg^{2+} in the support chemical composition shifts the reduction peak(s) towards higher temperatures. This leads to the conclusion that addition of Mg^{2+} in the present $Ce_{0.15}Zr_{0.85}O_2$ matrix increases its M–O–M and M–O–M′ (M, M′ different metal cations) bonds strength regarding surface and bulk oxygen.

The area under the TPR profile is directly proportional to the amount of labile lattice oxygen reacted with hydrogen to produce water. It was found that $Ce_{0.15}Zr_{0.83}Mg_{0.02}O_2$ and $Ce_{0.14}Zr_{0.81}Mg_{0.05}O_2$ consist of a larger amount (340 and 358 μmol/g, respectively) of labile oxygen compared to $Ce_{0.15}Zr_{0.85}O_2$ (263 μmol/g). Thus, the presence of Mg^{2+} in an amount of 2–5 atom% results in a significant increase in the reducibility of Ce–Zr–Mg–O solid solution. Similar observations were made by Wang et al. [41] who showed that the presence of Si in an amount of 5–10 wt% increased the reducibility of Ce–Zr–O solid.

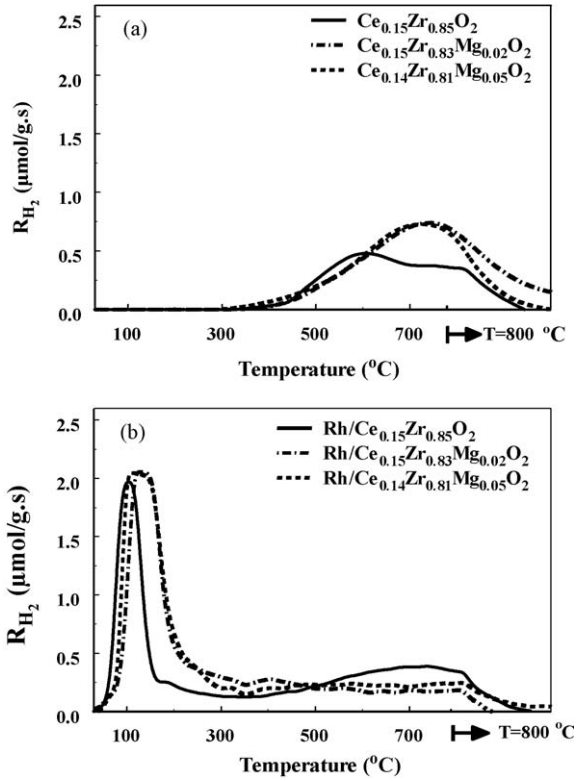

Fig. 1. H_2-TPR traces in terms of rate of hydrogen consumption (μmol H_2/g s) versus temperature obtained on (a) $Ce_{0.15}Zr_{0.85}O_2$, $Ce_{0.15}Zr_{0.83}Mg_{0.02}O_2$ and $Ce_{0.14}Zr_{0.81}Mg_{0.05}O_2$, and (b) 0.5% Rh/$Ce_{0.15}Zr_{0.85}O_2$, 0.5% Rh/$Ce_{0.15}Zr_{0.83}Mg_{0.02}O_2$ and 0.5% Rh/$Ce_{0.14}Zr_{0.81}Mg_{0.05}O_2$ solids. $F_{H2/He}$ = 30 N mL/min; β = 30 °C/min; $W_{(a)}$ = 0.5 g; $W_{(b)}$ = 0.2 g.

In the case of supported-Rh catalysts (Fig. 1b), H_2-TPR traces appear to lower temperatures compared to those observed in the support alone (Fig. 1a), and at the same time the characteristic H_2-TPR features of support alone observed in the 500–800 °C range have changed significantly. This is due to the presence of noble metal (Rh), where during H_2-TPR hydrogen activation by the Rh metal (active H formation) and subsequent migration to the support (spillover) favours reduction of support at lower temperatures [48–50].

As shown in Fig. 1b, all supported-Rh catalysts led to the formation of a well-resolved peak in the 25–200 °C range. In particular, a large narrow peak centered at 106, 136, and 126 °C was seen in the Rh/$Ce_{0.15}Zr_{0.85}O_2$, Rh/$Ce_{0.15}Zr_{0.83}Mg_{0.02}O_2$, and Rh/$Ce_{0.14}Zr_{0.81}Mg_{0.05}O_2$ catalysts, respectively. These peaks are attributed to both the reduction of rhodium oxide (Rh_2O_3) formed during pre-treatment with O_2/He at 600 °C and the reduction of surface Ce^{4+} species. The latter is true given the fact that the three catalysts have the same Rh loading (0.5 wt%) and, thus, the same amount of H_2 consumed would be expected for Rh_2O_3 reduction. Fornasiero et al. [51] have observed a H_2-TPR peak centred at 77 °C over Rh/CeO_2, Rh/ZrO_2 and Rh/$Ce_xZr_{1-x}O_2$ solids. A rather broad H_2-TPR trace in the 250–800 °C range for all three Rh-based catalysts was observed (Fig. 1b) due to different kinds of surface and bulk labile oxygen species present in the solids.

The quantity of labile oxygen species reacted with hydrogen estimated for the Rh/$Ce_{0.15}Zr_{0.85}O_2$, Rh/$Ce_{0.15}Zr_{0.83}Mg_{0.02}O_2$ and Rh/$Ce_{0.14}Zr_{0.81}Mg_{0.05}O_2$ catalysts was found to be 634, 628 and 681 μmol/g, respectively. In the case of Mg-containing catalysts a nearly twice amount of H_2 is consumed at low temperatures (25–250 °C) compared to the Rh/$Ce_{0.15}Zr_{0.85}O_2$ catalyst (Fig. 1b), suggesting the favoring role of Mg^{2+} in increasing the reducibility of Ce–Zr–Mg–O support *at low temperatures*.

3.1.5. CO_2 chemisorption at 25 °C followed by TPD over Ce–Zr–Mg–O mixed metal oxides

Fig. 2 presents CO_2–TPD profiles obtained on the pre-calcined $Ce_{0.15}Zr_{0.85}O_2$, $Ce_{0.15}Zr_{0.83}Mg_{0.02}O_2$ and $Ce_{0.14}Zr_{0.81}Mg_{0.05}O_2$ solids following chemisorption from a 3 vol.% CO_2/He gas mixture at room temperature. As seen in Fig. 2, $Ce_{0.15}Zr_{0.85}O_2$ and $Ce_{0.15}Zr_{0.83}Mg_{0.02}O_2$ led to the formation of CO_2 desorption at temperatures lower than about 320 °C. In the case of $Ce_{0.15}Zr_{0.85}O_2$ a distinct single CO_2 desorption peak was observed with peak maximum at 92 °C, which corresponds to a weak basic site, and a shoulder at the falling part of it. It was reported that CeO_2 exhibits weak and moderate basic sites compared to ZrO_2 [52,53], where the amount of basic sites in the latter solid is proportional to the percent of tetragonal phase ZrO_2 in the solid, whereas it is

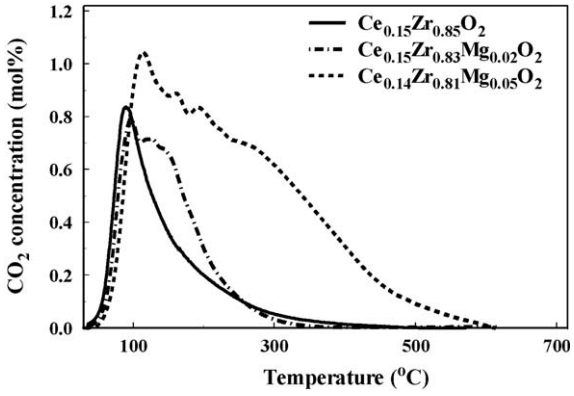

Fig. 2. CO_2–TPD response curves obtained under He flow over the $Ce_{0.15}Zr_{0.85}O_2$, $Ce_{0.15}Zr_{0.83}Mg_{0.02}O_2$ and $Ce_{0.14}Zr_{0.81}Mg_{0.05}O_2$ mixed metal oxides. Q_{He} = 30 N mL/min; β = 30 °C/min; W = 0.5 g.

independent of the CeO_2 crystal phase [53]. In the case of CeO_2–ZrO_2 mixed oxides the amount of basic sites decreases with increasing CeO_2 content [52]. It was reported that surface OH sites leads to the formation of hydrogen carbonate and is mainly observed in ceria-rich $Ce_xZr_{1-x}O_2$ solid solutions [54], not the present case of $Ce_{0.15}Zr_{0.85}O_2$. The observed desorption profile of CO_2 is therefore due to the surface O^{2-} basic sites that leads to carbonate species formation.

After adding 2 atom% Mg^{2+} ($Ce_{0.15}Zr_{0.83}Mg_{0.02}O_2$) two discernable CO_2 desorption peaks centred at 99 and 143 °C are observed with a shoulder at the falling part of the high-temperature peak, the magnitude of which increased with respect to the $Ce_{0.15}Zr_{0.85}O_2$ solid. By further increasing the Mg^{2+} content to 5 atom% but keeping practically the Ce/Zr ratio the same, more intense CO_2 desorption peaks were observed (Fig. 2, $Ce_{0.14}Zr_{0.81}Mg_{0.05}O_2$ solid) with peak maxima at 117, 165 and 195 °C accompanied by a large and broad shoulder at the falling part of the high-temperature peak. It is clearly illustrated that addition of Mg^{2+} in the Ce–Zr–O solid increases both the amount and strength of the surface basic sites of the material formed. There is apparently a redistribution of electron density on the surface oxygen atoms of $Ce_{0.15}Zr_{0.85}O_2$ after introducing Mg^{2+} in the crystal lattice. The increase of electron density on the surface oxygen atoms as reflected by the increase in the binding energy of adsorbed CO_2 is in harmony with the increase of Rh dispersion as previously discussed (see Section 3.1.3).

The concentration of the basic sites was estimated after integrating the CO_2–TPD curves up to 700 °C (Fig. 2), where no desorption of CO_2 was seen up to 800 °C. The surface basicity order obtained is as follows: $Ce_{0.14}Zr_{0.81}Mg_{0.05}O_2$ (202 μmol/g) > $Ce_{0.15}Zr_{0.83}Mg_{0.02}O_2$ (72 μmol/g) > $Ce_{0.15}Zr_{0.85}O_2$ (66.5 μmol/g). This order is correlated with the increase in the specific surface area ($m^2\ g^{-1}$) of the solids (Table 1) as one might expect.

3.1.6. CO_2 chemisorption at 25 °C followed by TPD over supported-Rh catalysts

CO_2–TPD experiments following *different reduction temperatures in hydrogen* applied over the supported-Rh catalysts was performed in order to investigate the effect of oxygen vacancies formed on the support surface on the CO_2 chemisortion and desorption behaviour (Fig. 3). Significant differences in the concentration and bonding strength of adsorbed CO_2 were observed. As seen in Fig. 3a, a single desorption peak (T_M = 106 °C) with a shoulder on the falling part of it (200–500 °C, likely associated with a different chemisorption site) was recorded for the $Rh/Ce_{0.15}Zr_{0.85}O_2$ solid after reduction at 300 °C, absent in the case of reduction in hydrogen at 200 °C (Fig. 2). By increasing the reduction temperature to 500 or 700 °C a small broad peak (T_M = 520 °C) was recorded which was not observed in the case of 300 °C reduction temperature. The CO_2 desorption peak observed at low temperatures could be assigned to adsorbed monodentate carbonate, whereas that detected at 520 °C could be assigned to adsorbed bidentate carbonate on oxygen vacancies [55–57].

The amounts (μmol/g) of CO_2 and CO (response curves not shown in Fig. 3) desorbed from the surface of $Rh/Ce_{0.15}Zr_{0.85}O_2$ catalyst are reported in Table 2. The amount of CO_2 decreases with increasing reduction temperature in the 300–700 °C range, while the opposite trend was found for the desorbed CO. It is well known that surface and subsurface oxygen vacancies can be formed in the present catalyst carrier after hydrogen reduction above 200 °C [58,59], and that CO_2 reacts predominantly with surface O^{2-} and OH species of a metal oxide forming carbonates and hydrogen carbonates, respectively [57,60]. An increase in reduction temperature leads to an increase in the concentration of surface oxygen vacancies which are offered to dissociate CO_2 into CO and lattice oxygen, and/or surface carbon [48,56,58]. The former precisely reflects the observed increase in CO formation with increasing H_2 reduction temperature of the catalyst (see Table 2) as also reported by others [61,62].

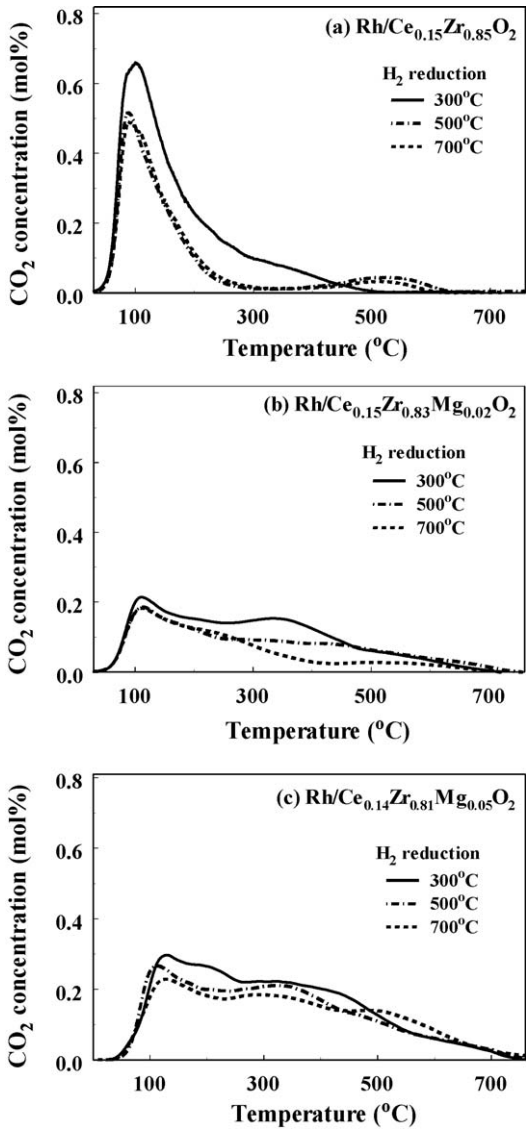

Fig. 3. CO_2–TPD response curves obtained over (a) $Rh/Ce_{0.15}Zr_{0.85}O_2$, (b) $Rh/Ce_{0.15}Zr_{0.83}Mg_{0.02}O_2$ and (c) $Rh/Ce_{0.14}Zr_{0.81}Mg_{0.05}O_2$ catalysts following CO_2 adsorption at 25 °C after catalyst calcination at 600 °C followed by H_2 reduction at 300, 500 and 700 °C. Q_{He} = 30 N mL/min; β = 30 °C/min; W = 0.5 g.

Table 2
Amounts (μmol/g) of CO_2 and CO desorbed from the surface of supported-Rh catalysts during CO_2–TPD studies following different catalyst H_2 reduction pretreatments.

Catalyst	Reduction temperature (°C)	Amount of CO_2 desorbed (μmol/g)	Amount of CO desorbed (μmol/g)
0.5% $Rh/Ce_{0.15}Zr_{0.85}O_2$	300	65	14
	500	46	26
	700	47	35
0.5% $Rh/Ce_{0.15}Zr_{0.83}Mg_{0.02}O_2$	300	54.7	10.1
	500	43.9	24.4
	700	33	37.9
0.5% $Rh/Ce_{0.14}Zr_{0.81}Mg_{0.05}O_2$	300	88	9
	500	78.3	15.6
	700	75.1	20.7

The CO_2–TPD response curves obtained on the Rh/$Ce_{0.15}Zr_{0.83}Mg_{0.02}O_2$ catalyst following reduction at 300 °C (Fig. 3b) consisted of two main and rather broad CO_2 desorption peaks (T_M = 111 and 340 °C) extended to 700 °C, not the case with the Rh/$Ce_{0.15}Zr_{0.85}O_2$ catalyst. After comparing the CO_2 desorption curves recorded following reduction at 300, 500 and 700 °C (Fig. 3b), and considering the results reported in Table 2, it is concluded that the increase in reduction temperature causes some changes in the shape but not the position of the whole CO_2 desorption curve, and a decrease in the amount of CO_2 and a simultaneous increase in the amount of CO desorbed. The latter was also observed in the case of Rh/$Ce_{0.15}Zr_{0.85}O_2$ and Rh/$Ce_{0.14}Zr_{0.81}Mg_{0.05}O_2$ catalysts (see Fig. 3a and c, respectively, and Table 2). The quantitative results shown in Table 2 (sum of CO_2 + CO formed) are in good agreement with the basicity results reported in the previous Section 3.1.5 (see also Fig. 2).

Jin et al. [63] reported on the CO and CO_2 chemisorption on 2 wt% Pt/CeO_2 catalyst. Based on their study CO_2 was adsorbed on a lattice oxygen vacancy of ceria support and decomposed to CO, provided that a metal atom (Rh in our case) is nearby to accept the CO, and, thereby filling the oxygen vacancy. It was assumed that the active site is present at the interface between Rh and the oxide support. Based on the results of Fig. 3 and Table 2, the amount of CO_2 and CO desorbed depends not only on the reduction temperature but also on the support chemical composition. An interesting observation is the fact that Rh/$Ce_{0.14}Zr_{0.81}Mg_{0.05}O_2$ catalyst led to significantly higher amounts of CO_2 and lower amounts of CO desorbed when reduction took place at 700 °C compared to the Rh/$Ce_{0.15}Zr_{0.85}O_2$ and Rh/$Ce_{0.15}Zr_{0.83}Mg_{0.02}O_2$ catalysts (Table 2).

3.1.7. CO chemisorption at 25 °C followed by TPD

Fig. 4a and b present CO_2 and CO–TPD response curves obtained over the 0.5% Rh/$Ce_{0.15}Zr_{0.85}O_2$, Rh/$Ce_{0.15}Zr_{0.83}Mg_{0.02}O_2$ and Rh/$Ce_{0.14}Zr_{0.81}Mg_{0.05}O_2$ catalysts following CO chemisorption at 25 °C (see Section 2.2.5). Molecular hydrogen in smaller concentrations than CO (Fig. 4b) was also observed (not shown in Fig. 4) as the result of the following reaction (4) between adsorbed CO on Rh with surface hydroxyl groups of the metal–oxide support located along the metal–support interface [64,65]:

$$CO_{ads} + OH_L \rightarrow CO_2(g) + (1/2)H_2(g) \quad (5)$$

This reaction route was confirmed in the present work via *in situ* CO chemisorption DRIFTS studies to be presented in Section 3.3.1.

The formation of CO_2 could also be the result of Boudouard reaction on the Rh surface [66,67]:

$$2CO\text{-}s \leftrightarrow CO_2 + C\text{-}s + s \quad (6)$$

The latter route was probed as follows. After CO–TPD (700 °C in He flow) the feed gas was changed to 20% O_2/He for the measurement (isothermal oxygen titration) of accumulated "carbon" species according to reaction (6) [68]. As shown in Fig. 4c, CO and CO_2 are formed, the amount of which was found to be 3.8 μmol "C"/g in the case of Rh/$Ce_{0.14}Zr_{0.81}Mg_{0.05}O_2$ catalyst.

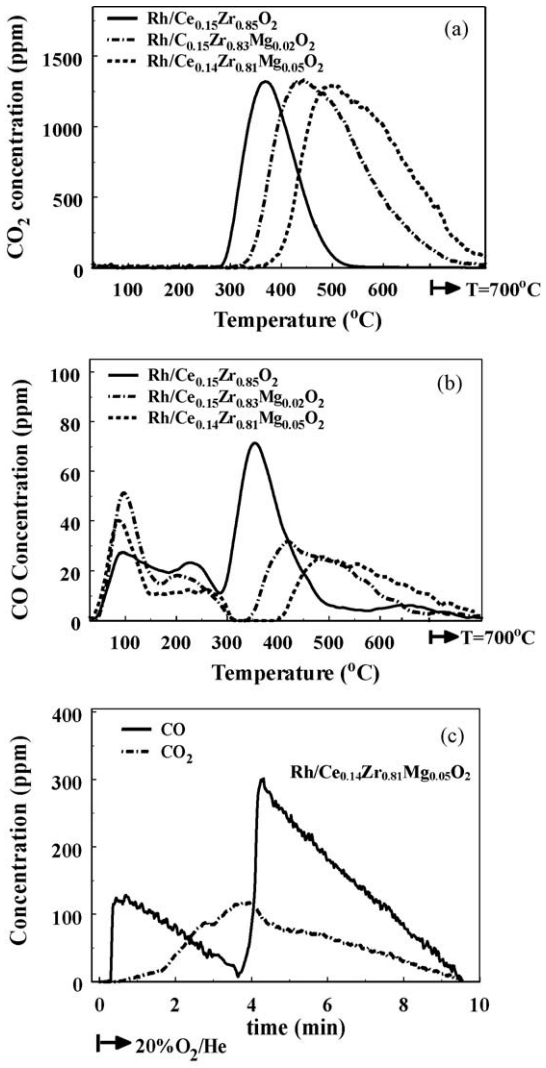

Fig. 4. TPD response curves of CO_2 (a) and CO (b) obtained over the Rh/$Ce_{0.15}Zr_{0.85}O_2$, Rh/$Ce_{0.15}Zr_{0.0.83}Mg_{0.02}O_2$ and Rh/$Ce_{0.14}Zr_{0.81}Mg_{0.05}O_2$ catalysts following CO chemisorption at 25 °C. Q_{He} = 30 N mL/min; β = 30 °C/min; W = 0.5 g. Also shown (c) are the transient response curves of CO and CO_2 obtained during isothermal oxygen titration at 700 °C of the "carbon" formed at the end of the CO–TPD run over the Rh/$Ce_{0.14}Zr_{0.81}Mg_{0.05}O_2$ catalyst.

Based on the amount of carbon formed, the above-mentioned for the reaction route (5), and the observed amount of CO_2 desorbed (Fig. 4a, Table 3), there must be a third reaction route for the formation of CO_2. The latter is suggested to be the reaction of adsorbed CO with lattice oxygen located at the metal–support interface according to reaction (7) [69]. In the latter reaction, $\square_L$ presents a lattice oxygen vacant site:

$$CO + O_L \leftrightarrow CO_2 + \square_L \quad (7)$$

Table 3
Amounts (μmol/g) of CO and CO_2 desorbed from the surface of supported-Rh catalysts investigated during CO–TPD studies. The peak maximum desorption temperatures (T_M) of the CO response curves are also given.

Catalyst	T_M (1) (°C)	T_M (2) (°C)	T_M (3) (°C)	Amount of CO desorbed (μmol/g)	Amount of CO_2 desorbed (μmol/g)
0.5% Rh/$Ce_{0.15}Zr_{0.85}O_2$[a]	98	230	357	1.02	13.1
0.5% Rh/$Ce_{0.15}Zr_{0.83}Mg_{0.02}O_2$[b]	96	200	400	0.95	16.2
0.5% Rh/$Ce_{0.14}Zr_{0.81}Mg_{0.05}O_2$[c]	89	200	480	0.81	15.5

[a] D = 25% (12.1 μmol Rh_s/g).
[b] D = 70% (34.0 μmol Rh_s/g).
[c] D = 76% (36.9 μmol Rh_s/g),

This reaction route finds also support by the CO formed at high temperatures ($T > 500$ °C) (Fig. 4b) based on the CO_2–TPDs previously reported (Fig. 3) and discussed.

The CO desorption temperatures at peak maxima (T_M) and the corresponding amounts of CO and CO_2 desorbed for all three supported-Rh catalysts are reported in Table 3. In all cases three main CO desorption peaks were found in the temperature range of 25–500 °C due to molecular desorption from the Rh surface, while desorption of small amounts of CO at $T > 500$°C is likely the result of dissociation of CO_2 formed at lower temperatures on oxygen vacancies (see reaction (6)). The above CO–TPD results illustrate that at least three different kinds of adsorbed CO are formed on the Rh surface, result that is in good agreement with *in situ* DRIFTS studies (see Section 3.3) and others reported [70]. These three CO species are assigned to linear, gem-dicarbonyl and bridged CO. It is noted that the increase in the Mg^{2+} content (0–5 atom%) of support leads to an increase in the desorption temperature of the strongly bound CO ($T > 300$ °C) (Table 3), which is also true for the desorbed CO_2 (Fig. 4), in full agreement with the CO_2–TPDs of Fig. 2. In the case of Rh/$Ce_{0.14}Zr_{0.81}Mg_{0.05}O_2$ catalyst, the results of Table 3 and that of Fig. 4c provide an amount of 23.9 μmol CO/g of catalyst adsorbed. This amount is equivalent to a surface coverage of $\theta = 0.65$ (based on CO/$Rh_s = 1$), suggesting the presence of bridged CO, as proved by the *in situ* DRIFTS–CO chemisorption studies (see Section 3.3.1).

3.1.8. Oxygen storage capacity (OSC) measurements

The OSC and OSCC (μmol O/g) of the three supported-Rh catalysts investigated in the present work were measured in the 350–550 °C range and results are reported in Table 4. Both quantities increase with temperature at which oxygen storage and release took place (see Section 2.2.6), while the positive effect of the presence of Mg^{2+} in the Ce–Zr–Mg–O solid solution is apparent in the whole temperature range of 350–550 °C. For example, at the lowest temperature of 350 °C the OSCC was increased by a factor of 1.8, while at the highest temperature of 550 °C by a factor of 1.2 after introducing 5 atom% Mg^{2+} in the Ce–Zr–O crystal structure. Similarly, in the case of OSC an increase by a factor of 1.8 and 1.6, respectively was observed at 350 and 500 °C (Table 4). These results are in harmony with the H_2-TPR results (Fig. 1b) presented and discussed in the previous Section 3.1.4. Again it is demonstrated that introduction of Mg^{2+} in the Ce–Zr–O lattice has increased both the surface and bulk oxygen mobility, and likely the site density of oxygen vacant sites.

3.2. Catalytic performance of supported-Rh catalysts

The steam reforming of phenol was studied in the 350–550 °C range over the supported-Rh catalysts described in Section 2.3.

Table 4
OSC and OSCC (μmol O/g) measured in the 350–550 °C range over the three supported-Rh catalysts investigated.

Catalyst	T (°C)	OSC (μmol O/g)	OSCC (μmol O/g)
0.5 wt% Rh/$Ce_{0.15}Zr_{0.85}O_2$	350	288	354
	400	309	397
	450	328	472
	550	365	615
0.5 wt% Rh/$Ce_{0.15}Zr_{0.83}Mg_{0.02}O_2$	350	365	483
	400	390	519
	450	412	572
	550	471	657
0.5 wt% Rh/$Ce_{0.14}Zr_{0.81}Mg_{0.05}O_2$	350	518	645
	400	532	663
	450	552	692
	550	598	752

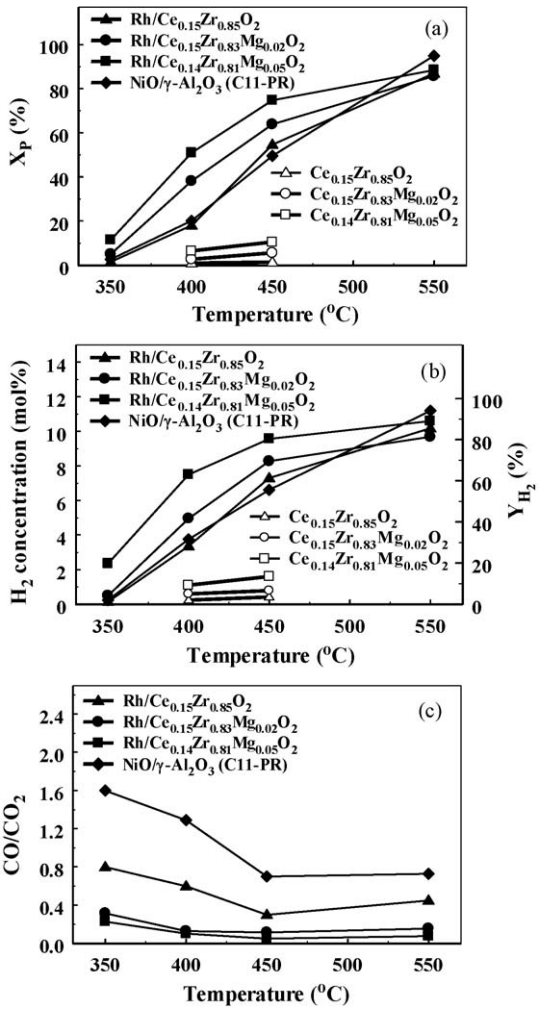

Fig. 5. Dependence of (a) phenol conversion, X_P (%), (b) hydrogen production (mol% dry-basis) and H_2-yield (%), and (c) CO/CO_2 product ratio on reaction temperature for the Rh/$Ce_{0.15}Zr_{0.85}O_2$, Rh/$Ce_{0.15}Zr_{0.83}Mg_{0.02}O_2$, Rh/$Ce_{0.14}Zr_{0.81}Mg_{0.05}O_2$ and a commercial Ni-based catalyst. Corresponding results for the Ce–Zr–Mg–O supports alone are also shown in (a) and (b). Feed composition: 0.6 vol.% C_6H_5OH/40 vol.% H_2O/59.4 vol.% He; $W_{cat} = 0.3$ g; $F_T = 200$ N mL/min; GHSV ~ 54,000 (h^{-1}).

Fig. 5a–c present the effect of reaction temperature on phenol conversion, X_P (%), hydrogen product concentration (mol%, dry-basis) and yield (see Section 2.3), and CO/CO_2 product ratio, respectively, obtained over Rh/$Ce_{0.15}Zr_{0.85}O_2$, Rh/$Ce_{0.15}Zr_{0.83}Mg_{0.02}O_2$, Rh/$Ce_{0.14}Zr_{0.81}Mg_{0.05}O_2$ and a commercial Ni-based catalyst (44 wt% NiO/γ-Al_2O_3, Sud-Chemie, code C11-PR) used in tar steam reforming reactions. The activity in terms of phenol conversion and hydrogen production obtained at 400 and 450 °C over the $Ce_{0.15}Zr_{0.85}O_2$, $Ce_{0.15}Zr_{0.83}Mg_{0.02}O_2$ and $Ce_{0.14}Zr_{0.81}Mg_{0.05}O_2$ supports alone is also given (Fig. 5a and b). The Rh/$Ce_{0.15}Zr_{0.81}Mg_{0.05}O_2$ catalyst shows significantly higher conversion values in the 350–450 °C range compared to the other catalysts studied, and the order of catalytic activity obtained in this temperature range was: Rh/$Ce_{0.14}Zr_{0.81}Mg_{0.05}O_2$ > Rh/$Ce_{0.15}Zr_{0.83}Mg_{0.02}O_2$ > Rh/$Ce_{0.15}Zr_{0.85}O_2$ ~ Ni-based (C11-PR) catalyst. At the highest reaction temperature of 550 °C, the four catalysts showed small variations in phenol conversion (Fig. 5a) and H_2-yield (Fig. 5b), with the industrial catalyst being slightly better.

It is remarkable that at 450 °C the Rh/$Ce_{0.14}Zr_{0.81}Mg_{0.05}O_2$ catalyst exhibits by 65% higher phenol conversion and by 75% higher H_2-yield compared to the Ni-based industrial catalyst, while the latter catalyst is only by 5% more active than the former

catalyst at 550 °C. It is also important to mention that the commercial catalyst has a Ni loading of ~44 wt% to be compared to the 0.5 wt% Rh used in the present work. We have previously reported [29] that 0.5 wt% Rh/MgO and 0.1 wt% Rh/Mg–Ce–Zr–O catalysts both synthesized by the sol–gel method and tested in the 575–730 °C range exhibited also better performance towards steam reforming of phenol when compared to the same commercial Ni-based catalyst.

Frusteri et al. [71] have shown that Rh/MgO exhibits better performance both in terms of activity and stability compared to Ni/MgO for the steam reforming of simulated bio-ethanol at 650 °C. In addition, Rh/MgO was observed to be more resistant towards coke formation compared to the Ni/MgO catalyst. Research works conducted by Asadullah and Tomishige [23–28] towards steam reforming of tar compounds derived during biomass gasification over $M/CeO_2–SiO_2$ (M = Rh, Pt, Pd, Ru, Ni) in the 550–650 °C range led to the following order of activity: Rh > Pd > Ni ~ Pt. On the other hand, the activity of Ni at $T > 650$ °C was found to be higher than of Pd [23]. These results are in good agreement with the present results regarding the steam reforming of phenol conducted in a lower temperature range (Fig. 5a and b).

By comparing the catalytic activity of support alone and that obtained from the corresponding supported-Rh catalyst (Fig. 5a and b), it is illustrated that the activity of supported-Rh is largely due to the presence of Rh metal. Furthermore, the reforming activity is found to be favoured over small Rh particles (the case of Mg-containing supported-Rh catalysts), and this is largely influenced by the support chemical composition.

Fig. 5b presents the hydrogen yield (Y_{H2}, %) as a function of reaction temperature (350–550 °C) for the steam reforming of phenol over the three supported-Rh catalysts and the Ni-based commercial one (C11-PR). At 450 °C, nearly 85% of the maximum hydrogen production expected (see Section 2.3, Eq. (4)) was obtained on the $Rh/Ce_{0.14}Zr_{0.81}Mg_{0.05}O_2$ catalyst and only 55% on the commercial Ni-based catalyst (Fig. 5b). Considering the relatively high GHSV (h^{-1}) used in the present catalytic experiments, maximum hydrogen yields seem possible to be obtained over the present $Rh/Ce_{0.14}Zr_{0.81}Mg_{0.05}O_2$ novel catalytic system at 450 °C. The effect of GHSV on phenol conversion at 350 and 550 °C is presented in the following Section 3.2.3.

3.2.1. Intrinsic reasons for the positive effect of the presence of Mg^{2+} in support composition (Ce–Zr–Mg–O) on catalyst performance

As previously shown (Fig. 5) the incorporation of Mg^{2+} ions in the crystal structure of $Ce_{0.15}Zr_{0.85}O_2$ solid solution at the level of 5 atom% was largely beneficial for the phenol steam reforming activity in the 350–450 °C low-temperature range. One of the most important intrinsic reasons for this behaviour is suggested to be the increase of support surface basicity with increasing Mg^{2+} content (Fig. 2), in terms of concentration of basic sites (O^{n-}) with suitable electron charge density. Duprez et al. [72] proposed a bi-functional mechanism for the steam reforming of aromatics, where the aromatic molecule is activated on the metal particle and the water molecule on the support, the latter leading to the formation of hydroxyl groups. This mechanism was also found strong support by the work of Polychronopoulou et al. [73] in the case of steam reforming of phenol over supported-Rh and Fe/Mg–Ce–O catalysts based on transient isotopic experiments, where the back-spillover of labile O and OH species from the support to the metal–support interface was proven to take place, thus consisting an important step in the mechanism of phenol steam reforming towards H_2, CO and CO_2 formation.

The above-offered discussion on the participation of labile O and OH species from the support to the metal–support interface should be considered when trying to understand the effect of basicity of support on the activity of the present supported-Rh catalysts. The following is aimed to addressing this important fundamental issue.

(a) The H_2-TPR results of Fig. 1 and those of OSC (Table 4) illustrate that the presence of 5 atom% Mg^{2+} in the $Ce_{0.14}Zr_{0.81}Mg_{0.05}O_2$ structure significantly enhances the concentration of oxygen species reacting with hydrogen at temperatures in the 300–550 °C range. Thus, the presence of Mg^{2+} resulted in the lowering of binding energy of surface oxygen in the M–O–M and M–O–M′ moieties.

(b) Selective CO_2 chemisorption followed by TPD (Fig. 2) illustrate the significant increase in the number of surface basic sites (O^{n-}), where an increase by a factor of three was measured by adding 5 atom% Mg^{2+} into the $Ce_{0.15}Zr_{0.85}O_2$ solid structure. It is well known [74] that metal oxides of basic character largely promote water dissociation leading to the formation of –OH species. The latter, as previously discussed is considered key active species for the steam reforming of phenol reaction. Rioche et al. [75] have shown that the use of ceria-zirconia leads to higher H_2-yields compared to the case of alumina-supported catalysts for steam reforming in the 650–950 °C range. Also, Polychronopoulou et al. [29] showed that 0.5 wt% Rh supported on 50Mg–25Ce–25Zr–O mixed metal oxide synthesized by the sol–gel method presented almost two times higher specific integral rates of hydrogen production in the 575–730 °C range compared to 0.5 wt% Rh supported on ZrO_2, the latter catalyst also synthesized by the sol–gel method, for the steam reforming of phenol.

(c) Catalytic results regarding the WGS reaction obtained over the present supported-Rh catalysts to be presented next illustrate the increased activity of $Rh/Ce_{0.14}Zr_{0.81}Mg_{0.05}O_2$ compared to $Rh/Ce_{0.15}Zr_{0.85}O_2$. The latter result shows that surface basicity has influenced to a positive manner the WGS reaction being an important reaction for hydrogen yield maximisation (Fig. 5b) in the steam reforming of phenol. The increase of Mg^{2+} content (0–5 atom%) was found to lead to a significant decrease in the CO/CO_2 product ratio (Fig. 5c). In particular, the CO/CO_2 product ratio drop compared to the commercial Ni-based catalyst becomes remarkable in the 350–450 °C range. As will be shown next, the fact that $Rh/Ce_{0.15}Zr_{0.81}Mg_{0.05}O_2$ demonstrates the lowest CO/CO_2 product ratio could be partly related to the higher concentration of cationic Rh^{n+} species present in the latter catalyst composition. A dramatic influence of catalyst composition on the CO/CO_2 product ratio was obtained by Diagne et al. [76,77] for ethanol steam reforming (300–500 °C) over 2 wt% Rh supported on CeO_2, ZrO_2 and $CeO_2–ZrO_2$ (Ce/Zr = 4, 2, and 1) solids, where $CeO_2–ZrO_2$ was found to be the best support with the highest H_2 and CO_2 production. It was also pointed out that the CO/CO_2 ratio was sensitive to the Ce/Zr ratio for the $Rh/CeO_2–ZrO_2$ catalyst.

(d) Carbon deposition measured after steam reforming of phenol, to be presented in the following Section 3.2.4, reveal the beneficial role of Mg^{2+} present in the $Ce_{0.14}Zr_{0.81}Mg_{0.05}O_2$ support composition. The positive role of MgO in favouring the rate of ethanol steam reforming and at the same time inhibiting coke formation was also reported [78].

(e) Based on the CO_2–TPD results of Fig. 3 obtained over the supported-Rh catalysts, there is a significant decrease in the amount of CO_2 desorbed at $T < 300$ °C (weak basic sites) upon introduction of Mg^{2+} ions in the structure of $Ce_{0.15}Zr_{0.85}O_2$ solid. It is likely that these specific basic sites (O^{n-}) favour dissociation of water, thus increasing the concentration of labile OH species, and in turn phenol steam reforming activity as previously discussed.

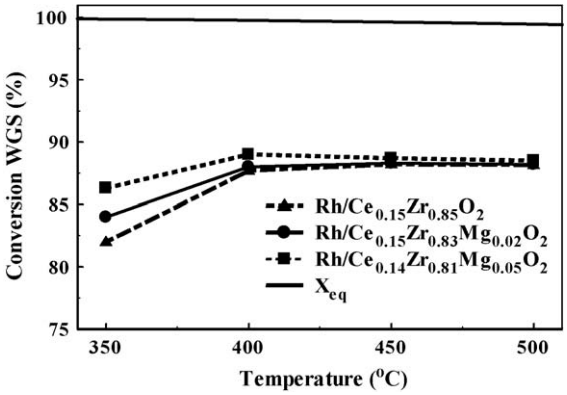

Fig. 6. Effect of reaction temperature on the conversion of CO obtained during WGS reaction over the $Rh/Ce_{0.15}Zr_{0.85}O_2$, $Rh/Ce_{0.15}Zr_{0.83}Mg_{0.02}O_2$, and $Rh/Ce_{0.14}Zr_{0.81}Mg_{0.05}O_2$ catalysts. Also shown is the CO conversion (X_{eq}) versus T curve estimated for equilibrium conditions. Feed composition: 1 vol.% CO/40 vol.% H_2O/59.0 vol.% He; W_{cat} = 0.3 g; F_T = 200 N mL/min; GHSV ~ 54,000 h^{-1}.

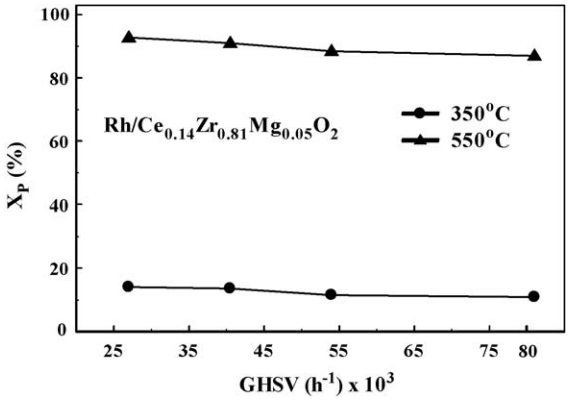

Fig. 7. Dependence of phenol conversion (X_P, %) on gas hourly space velocity (GHSV, h^{-1}) and reaction temperature for the $Rh/Ce_{0.14}Zr_{0.81}Mg_{0.05}O_2$ catalyst. Feed composition used: 0.6% C_6H_5OH/40% H_2O/59.4% He; W_{cat} = 0.3 g; T = 350 and 550 °C.

3.2.2. The water–gas shift reaction

Fig. 6 presents the effect of reaction temperature on the CO conversion, X_{CO} (%) of WGS reaction over the three supported-Rh catalysts using a feed composition of 1% CO/40% H_2O/He that simulates the composition in CO and H_2O encountered at the exit of reactor under steam reforming of phenol reaction conditions (Fig. 5). The CO conversion estimated under thermodynamic equilibrium conditions (X_{eq}, Fig. 6) is also given. This curve was derived using equilibrium constant (K_{eq}) values reported [79] and appropriate mass balances [39]. The equilibrium curve shows that full CO conversion can be achieved in the 350–550 °C range under the used feed composition (1% CO/40% H_2O/He). It is observed that the activity of all supported-Rh catalysts towards the WGS reaction is higher than 80%, where at the lowest reaction temperature of 350 °C the $Rh/Ce_{0.15}Zr_{0.81}Mg_{0.05}O_2$ catalyst exhibits about 5 percentage units higher conversion than the $Rh/Ce_{0.15}Zr_{0.85}O_2$. At higher reaction temperatures, all three catalysts exhibit practically similar WGS activity.

It is interesting to show here how close to equilibrium the WGS reaction was in the case of phenol steam reforming (Fig. 5) over the $Rh/Ce_{0.14}Zr_{0.81}Mg_{0.05}O_2$ catalyst. At 350 °C, using y_{H2} = 0.0235, y_{CO2} = 0.0052, y_{CO} = 0.0012 and y_{H2O} = 0.4 (y_i = mole fraction of gaseous species), and the theoretical equilibrium constant, $K_{WGS,th}$ = 20.45, it is estimated that the theoretical product $y_{CO2} \cdot y_{H2}$ equals 98.2×10^{-4}, while the corresponding experimental value was only 1.22×10^{-4}. On the other hand, at 550 °C it was found that the theoretical product $y_{CO2} \cdot y_{H2}$ equals 41×10^{-4}, while the corresponding experimental value was practically the same, 41.8×10^{-4} ($K_{WGS,th}$ = 3.43, y_{H2} = 0.106, y_{CO2} = 0.0394, y_{CO} = 0.0030, y_{H2O} = 0.4). These results clearly demonstrate that under the experimental conditions examined (Fig. 5), the WGS reaction was far from being at equilibrium at 350 °C but it was very close to equilibrium at 550 °C.

3.2.3. Effect of gas hourly space velocity (GHSV, h^{-1})

The effect of gas hourly space velocity (GHSV, h^{-1}) on phenol conversion, X_P (%) obtained over the $Rh/Ce_{0.14}Zr_{0.81}Mg_{0.05}O_2$ catalyst after 30 min on reaction stream at 350 and 550 °C is reported in Fig. 7. The phenol and water feed concentrations were kept constant at 0.6 and 40 vol.%, respectively, while the GHSV varied in the 25,000–80,000 h^{-1} range. It is clearly seen that phenol conversion shows only a slight gradual decrease with increasing GHSV (h^{-1}) for both reaction temperatures studied. This behaviour suggests that external mass transport resistances in the given powdered catalytic bed were kept minimum, and full conversion of phenol could be maintained after using a GHSV close to 20,000 h^{-1}.

3.2.4. Stability test and carbon deposition

Fig. 8 reports the performance in terms of H_2 product concentration (mol%, dry-basis) of the 0.5 wt% $Rh/Ce_{0.14}Zr_{0.81}Mg_{0.05}O_2$ catalyst with time on stream (stability test up to 12 h) under phenol steam reforming reaction at 550 °C (see Fig. 5b). The catalyst exhibits a remarkable stable performance with a H_2-yield of about 85% (or 10 mol% H_2 concentration, see also Fig. 5b). The amount of "carbon" accumulated after 2 h of continuous reaction was estimated after following an isothermal oxygen titration [68] experiment at 650 °C. Based on the CO and CO_2 transient response curves obtained and a carbon material balance, the amount of "carbon" was found to be 112 μmol C/g catalyst. Similar experiments conducted over the 0.5 wt% $Rh/Ce_{0.15}Zr_{0.85}O_2$ and 0.5 wt% $Rh/Ce_{0.15}Zr_{0.83}Mg_{0.02}O_2$ catalysts resulted in 173 and 149 μmol C/g catalyst, respectively. These amounts are equivalent to more than three equivalent surface Rh monolayers ($\theta_C > 3.0$) in all three catalysts, suggesting that likely part of this "carbon" must reside on the support.

3.3. In situ DRIFTS studies

3.3.1. Chemical structure of adsorbed CO on 0.5% $Rh/Ce_{0.15}Zr_{0.85}O_2$ and 0.5% $Rh/Ce_{0.14}Zr_{0.81}Mg_{0.05}O_2$ catalysts

Characterization of the kinds of adsorbed CO formed on the surface of the most and least active supported-Rh catalysts regarding the present steam reforming of phenol reaction was studied using *in situ* DRIFTS. The interaction between CO and

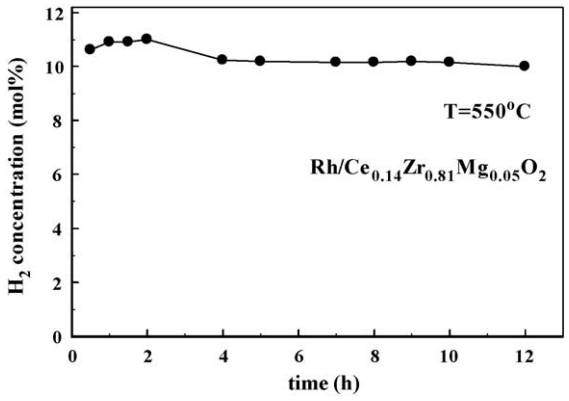

Fig. 8. Stability test of phenol steam reforming at 550 °C over the $Rh/Ce_{0.14}Zr_{0.81}Mg_{0.05}O_2$ catalyst. Feed composition used: 0.6% C_6H_5OH/40% H_2O/59.4% He; W_{cat} = 0.3 g; GHSV ~ 54,000 h^{-1}.

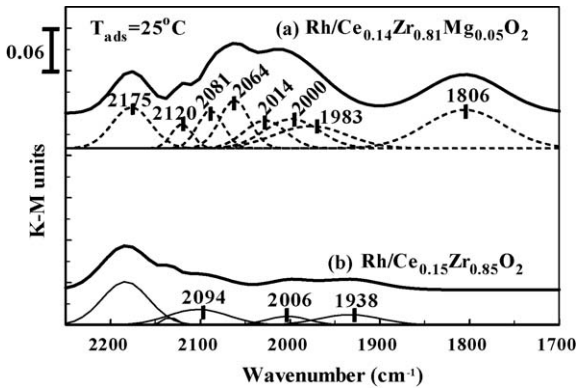

Fig. 9. *In situ* DRIFTS–CO spectra recorded in the 2250–1700 cm^{-1} range over (a) 0.5% $Rh/Ce_{0.14}Zr_{0.81}Mg_{0.05}O_2$ and (b) 0.5% $Rh/Ce_{0.15}Zr_{0.85}O_2$ catalysts. Adsorption of CO was conducted from a 2 vol.% CO/He gas mixture at 25 °C for 30 min following catalyst H_2 reduction at 200 °C.

supported-Rh surfaces produces three distinct CO adsorption modes: (a) dicarbonyl $Rh^+(CO)_2$ populated on cationic rhodium species, (b) linear bonded CO, Rh–CO, and (c) bridged bonded CO, Rh_2CO [70,80–84]. The adsorption and desorption behaviour of CO is influenced by the support, the Rh particle size, and the oxidation state of Rh [80,81,84,85]. As shown in Fig. 9, exposure of $Rh/Ce_{0.15}Zr_{0.85}O_2$ and $Rh/Ce_{0.15}Zr_{0.81}Mg_{0.05}O_2$ surfaces to CO after 30 min on 2% CO/He gas mixture led to the formation of IR bands in the 2100–1700 cm^{-1} range due exclusively to the adsorption of CO on Rh. The IR bands shown at 2175 and 2120 cm^{-1} (Fig. 9) following deconvolution (see Section 2.4.1) are due to gas-phase CO.

CO adsorption at 25 °C over the 0.5% $Rh/Ce_{0.14}Zr_{0.81}Mg_{0.05}O_2$ catalyst led to the formation of two strong IR bands at 2081 and 2014 cm^{-1} which are assigned to the asymmetric and symmetric stretching vibrational modes of $Rh^+(CO)_2$ species, respectively [80,84,86]. It is noted that the $\Delta\nu$ (C=O) shift observed between the symmetric and asymmetric stretching vibrational modes of gem-dicarbonyl (Fig. 9a) is 69 cm^{-1}, which is in the 60–75 cm^{-1} range previously reported [81,83,86]. It should be pointed out that this shift depends on the kind of support and Rh dispersion. As reported by Zhang et al. [85], formation of gem-dicarbonyl CO may involve the alteration and inter-conversion of linear and bridged bound CO species. Additionally, formation of this adsorbed CO may also suggest CO-induced disruption of Rh_x clusters, phenomenon reported to be fast on CeO_2-containing supported metal catalysts [87].

The IR absorption band observed at 2064 cm^{-1} corresponds to linear CO, while the broad IR band at 1806 cm^{-1} corresponds to bridged CO [80,88–90]. It is important to note that IR bands were also recorded in the 1700–1100 cm^{-1} spectral region (not shown here) corresponding to various carbonate species due to the formation of CO_2 likely via reactions (6) and (7). In the case of $Rh/Ce_{0.15}Zr_{0.85}O_2$ catalyst (Fig. 9b), three IR bands centred at 2094, 2006, and 1938 cm^{-1} are discernable. The IR bands centred at 2094 and 2006 cm^{-1} may be assigned to two different linear CO species, while the IR band at 1938 cm^{-1} to bridge-bonded CO [86,88,90].

According to the results of Fig. 9, the formation of gem-dicarbonyl was favoured on the Rh surface of the more active 0.5% $Rh/Ce_{0.14}Zr_{0.81}Mg_{0.05}O_2$ catalyst (Fig. 5). It was reported that the presence of increased concentration of cationic rhodium species is found in highly dispersed supported-Rh catalysts [86,91]. This is in agreement with the higher Rh dispersion estimated for the $Rh/Ce_{0.15}Zr_{0.81}Mg_{0.05}O_2$ compared to $Rh/Ce_{0.15}Zr_{0.85}O_2$ catalyst. It is known that the thermo-stability of adsorbed CO is in the order: bridged (Rh_2CO) > linear (RhCO) > gem-dicarbonyl ($Rh(CO)_2$) [92]. The latter along with the fact that a higher surface

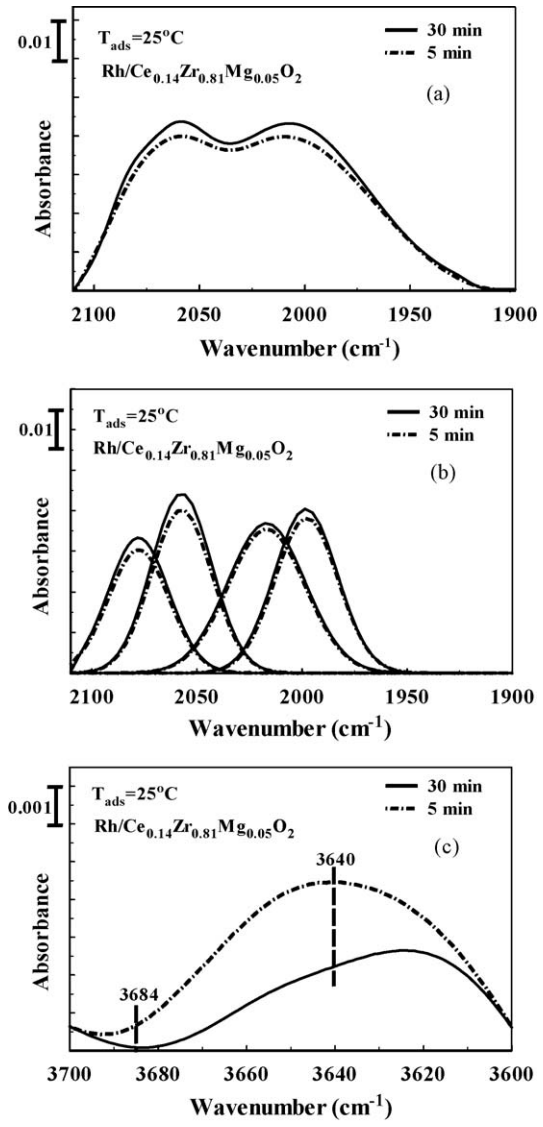

Fig. 10. (a) Evolution of the IR band in the 2100–1900 cm^{-1} range with time on CO adsorption (2 vol.% CO/He) at 25 °C, and (b) deconvolution of this IR band into two kinds of gem-dicarbonyl CO species. (c) Evolution of the IR band in the 3700–3600 cm^{-1} range with time on CO adsorption at 25 °C. Catalyst: 0.5% $Rh/Ce_{0.14}Zr_{0.81}Mg_{0.05}O_2$.

concentration of gem-dicarbonyl was found on $Rh/Ce_{0.14}Zr_{0.81}Mg_{0.05}O_2$ compared to 0.5% $Rh/Ce_{0.15}Zr_{0.85}O_2$ may suggest that the better activity of the former catalyst towards phenol steam reforming (Fig. 5) could be partly related to the presence of an increased concentration of Rh^{n+} cationic sites.

In order to provide more support on the presence of Rh^{n+} cationic sites as the result of the disruptive oxidation of Rh^o_x crystallites by–OH species located at the metal–support interface [93], we have followed with time on CO adsorption the evolution of infrared bands due to gem-dicarbonyl ($Rh(CO)_2$) and –OH species, and the obtained results are shown in Fig. 10. There is a clear increase in the intensity of the IR band recorded in the 2100–1900 cm^{-1} range (Fig. 10a) with increasing time on CO adsorption, and a concomitant decrease in the intensity of the IR band of –OH in the 3700–3600 cm^{-1} range (Fig. 10c) associated with the O–H stretching region. The latter is the result of the consumption of –OH species to form the gem-dicarbonyl CO adsorbed species and H_2 gas, according to the postulated mechanism for the formation of $Rh^I(CO)_2$ first reported by Basu et al. [93], and later on proved and adopted by many other researchers. In the present work the

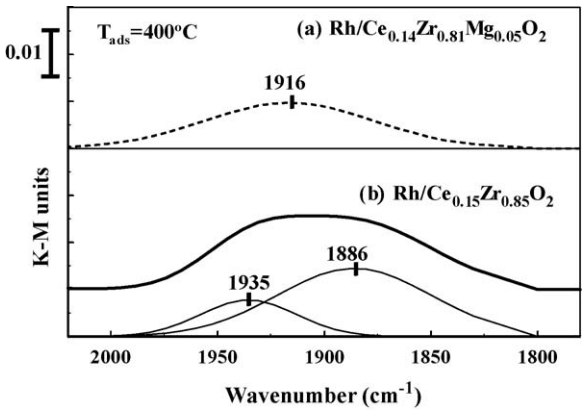

Fig. 11. *In situ* DRIFTS–CO spectra recorded in the 2050–1800 cm^{-1} range over (a) 0.5% Rh/$Ce_{0.14}Zr_{0.81}Mg_{0.05}O_2$ and (b) 0.5% Rh/$Ce_{0.15}Zr_{0.85}O_2$ catalysts following CO adsorption from a 2 vol.% CO/He gas mixture at 400 °C for 30 min after catalyst H_2 reduction at 200 °C.

infrared band associated with OH species of $Ce_{0.14}Zr_{0.81}Mg_{0.05}O_2$ oxidic support and which was found to diminish with time on CO adsorption was centred at 3640 cm^{-1} (Fig. 10c), similar to the value observed on Rh/Al_2O_3 (3675–3683 cm^{-1}) [93]. Fig. 10b shows the performed deconvolution in the 2100–1900 cm^{-1} region, where for the best curve fitting (Fig. 10a) two kinds of gem-dicarbonyl CO had been assigned with a ratio of integrated absorbance A_{asym}/A_{sym} = 1.15 [83].

Fig. 11 compares *in situ* DRIFTS–CO spectra recorded in the 2050–1850 cm^{-1} range (*K–M* units) after a 30-min treatment at 400 °C of the 0.5% Rh/$Ce_{0.14}Zr_{0.81}Mg_{0.05}O_2$ and 0.5% Rh/$Ce_{0.15}Zr_{0.85}O_2$ catalysts with a 2 vol.% CO/He gas mixture. In the case of Rh/$Ce_{0.14}Zr_{0.81}Mg_{0.05}O_2$ (Fig. 11a) the broad IR band observed at 1916 cm^{-1} is assigned to bridged bonded CO on Rh^0 [80,88–90], whereas two kinds of bridged bonded CO on Rh^0 (1935 and 1886 cm^{-1}) were noticed in the case of 0.5% Rh/$Ce_{0.15}Zr_{0.85}O_2$ catalyst (Fig. 11b). Additional IR bands were found in the 1700–1100 cm^{-1} range due to the presence of adsorbed carbonates in harmony with the CO–TPDs (Fig. 4). The DRIFTS–CO chemisorption results of Fig. 11 illustrate again the effect of support chemical composition on the kinds and relative population of adsorbed CO on Rh, where CO is a reaction product in the steam reforming of phenol reaction network. The fact that neither gem-dicarbonyl nor linear CO was detected on the surface of both catalysts (Fig. 11) may not strictly imply that Rh^{n+} cationic species are not present (see previous paragraph). This might be the result of the low thermal stability of gem-dicarbonyl CO compared to the linear and bridged adsorbed CO species [92]. A comparison between Figs. 9 and 11 shows that the increase of adsorption temperature from 25 to 400 °C favours the formation of bridged CO on the Rh surface. These results are in agreement with the fact that bridged CO is more thermally stable than linear and gem-dicarbonyl CO species [92].

3.3.2. *In situ DRIFTS–WGS reaction on 0.5% Rh/$Ce_{0.15}Zr_{0.85}O_2$ and 0.5% Rh/$Ce_{0.15}Zr_{0.81}Mg_{0.05}O_2$ catalysts*

In situ DRIFTS spectra in the 3100–1160 cm^{-1} range recorded over the Rh/$Ce_{0.15}Zr_{0.85}O_2$ and Rh/$Ce_{0.14}Zr_{0.81}Mg_{0.05}O_2$ catalysts after a 30 min of WGS reaction at 350 °C are shown in Fig. 12. A rapid built up of vibrational features associated with gas phase CO_2 (2353, 2317 cm^{-1}) were observed for both catalysts studied (Fig. 12a). The IR bands recorded at 2025 and 1830 cm^{-1} correspond to linear and bridged CO species, respectively [86,88,90]. In addition, the intense broad bands centered at 1560 and 1365 cm^{-1} are assigned to asymmetric and symmetric O–C–O stretching vibrational modes of formate species, while the

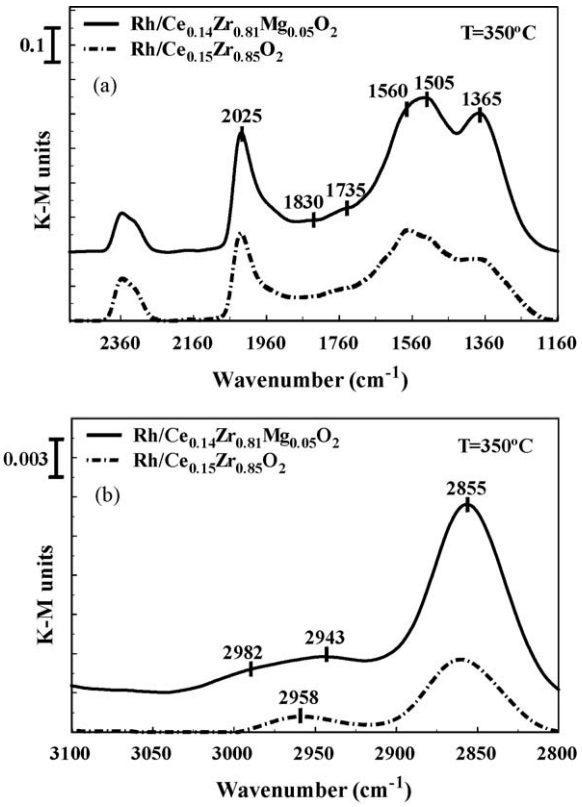

Fig. 12. *In situ* DRIFTS spectra recorded in the (a) 2500–1160 cm^{-1} and (b) 3100–2800 cm^{-1} range after 30 min of WGS reaction at 350 °C over the 0.5% Rh/$Ce_{0.14}Zr_{0.81}Mg_{0.05}O_2$ and 0.5% Rh/$Ce_{0.15}Zr_{0.85}O_2$ catalysts. Feed composition: 1 vol.% CO/40 vol.% H_2O/59 vol.% He; W_{cat} = 35 mg.

IR band at 1505 cm^{-1} to the OCO_{as} vibrational mode of unidentate carbonate which is associated with the basic surface O^{2-} sites of support [94,95]. The broad weak IR band centred at 1735 cm^{-1} is attributed to bridged carbonates formed on the $Ce_{0.15}Zr_{0.85}O_2$ and $Ce_{0.14}Zr_{0.81}Mg_{0.05}O_2$ support surfaces and unlikely to adsorbed water at 350 °C.

The IR spectrum in the 3100–2800 cm^{-1} range due to the stretching νCH and δCH + νOCO_a vibrational modes of formate (–COOH) species [96] is presented in Fig. 12b. A third small vibrational mode, δCH + νOCO_s due to the same kind of formate species (e.g., bidentate or bridged) is usually observed below 2800 cm^{-1} [96] and is not presented here. In the case of Rh/$Ce_{0.14}Zr_{0.81}Mg_{0.05}O_2$, the observed spectrum must be seen as consisting of at least three IR bands (Fig. 12b), which suggests the presence of *two kinds* of formate species. Given the chemical nature of this support surface, this is rather reasonable. Two kinds of formate species formed during the WGS reaction at 200 °C was evidenced in the case of Pt/TiO_2 catalyst [40]. On the other hand, in the case of Rh/$Ce_{0.15}Zr_{0.85}O_2$ catalyst one kind of formate species is rather formed (2958 and 2855 cm^{-1}, Fig. 12b).

In situ DRIFTS spectra were also recorded after 30 min of WGS reaction at 550 °C (Fig. 13). Very similar characteristic infrared bands to those recorded in the 2400–1160 cm^{-1} range at 350 °C (Fig. 12) are also observed. On the other hand, the kinds and number of formate species and their surface concentrations observed over both supported-Rh catalysts appear to be different (compare Figs. 12b and 13b). In particular, it is noted that the surface concentration of formate species at both WGS reaction temperatures appears to be larger on Rh/$Ce_{0.14}Zr_{0.81}Mg_{0.05}O_2$ than Rh/$Ce_{0.15}Zr_{0.85}O_2$ catalyst. It has been demonstrated using SSITKA–DRIFTS and other transient isotopic experiments that formate species could be considered as *active* or *inactive* reaction

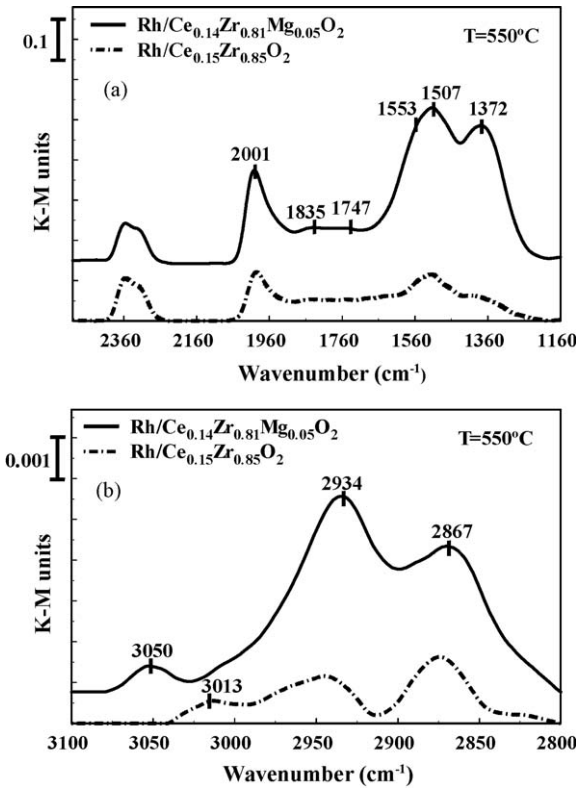

Fig. 13. *In situ* DRIFTS spectra recorded in the (a) 2500–1160 cm^{-1} and (b) 3100–2800 cm^{-1} range after 30 min of WGS reaction at 550 °C over the 0.5% Rh/$Ce_{0.14}Zr_{0.81}Mg_{0.05}O_2$ and 0.5% Rh/$Ce_{0.15}Zr_{0.85}O_2$ catalysts. Feed composition: 1 vol.% CO/40 vol.% H_2O/59 vol.% He; W_{cat} = 35 mg.

intermediate species of the WGS reaction over supported noble metals depending on the metal–oxide–support composition used [39,40]. It could therefore be proposed that the larger activity per gram basis of Rh/$Ce_{0.14}Zr_{0.81}Mg_{0.05}O_2$ compared to Rh/$Ce_{0.15}Zr_{0.85}O_2$ catalyst might be related to the increased surface concentration (μmol/g) of active formate species, the latter promoted by the presence of Mg^{2+} in the $Ce_{0.14}Zr_{0.81}Mg_{0.05}O_2$ support composition.

4. Conclusions

The following conclusions can be derived from the results of the present work:

(a) Addition of small amounts of Mg^{2+} (2–5 atom%) in the $Ce_{0.15}Zr_{0.85}O_2$ solid solution was found to promote the formation of well-dispersed supported-Rh catalysts (0.5 wt% Rh), the reducibility (weakening of M–O–M′ bonds strength), surface basicity, and oxygen storage capacity of Ce–Zr–Mg–O mixed metal oxide.

(b) An increase of reduction temperature in the 300–700 °C range in hydrogen flow over Rh/$Ce_{0.15}Zr_{0.85}O_2$, Rh/$Ce_{0.15}Zr_{0.83}Mg_{0.02}O_2$ and Rh/$Ce_{0.14}Zr_{0.81}Mg_{0.05}O_2$ catalysts resulted in a decrease in the amount (μmol/g) of desorbed CO_2 following CO_2–TPD, while the opposite is true for the amount of desorbed CO. The latter is related to the creation of oxygen vacancies that favour dissociation of CO_2 into CO and lattice oxygen.

(c) Low-temperature (350–550 °C) phenol steam reforming was proven to occur to a substantial extent over supported-Rh catalysts of low loading (0.5 wt%). The support chemical composition (Ce–Zr–Mg–O) was found to significantly improve the catalytic activity in the 400–500 °C range compared to the Ce–Zr–O support composition used to deposit the same amount of Rh metal.

(d) A 0.5 wt% Rh/$Ce_{0.14}Zr_{0.81}Mg_{0.05}O_2$ catalyst developed led to a significantly better performance towards steam reforming of phenol in terms of phenol conversion, H_2-yield and CO/CO_2 product ratio compared to a commercial Ni-based catalyst (44 wt% Ni) in the 350–450 °C temperature range. This catalyst composition shows an exceptional phenol conversion (∼90%) and H_2-yield (85%) for over 12 h of continuous phenol steam reforming reaction (0.6% C_6H_5OH/40% H_2O/He, GHSV = 54,000 h^{-1}) at 550 °C.

(e) *In situ* DRIFTS–CO chemisorption studies conducted over Rh/$Ce_{0.15}Zr_{0.81}Mg_{0.05}O_2$ and Rh/$Ce_{0.15}Zr_{0.85}O_2$ solids revealed the population of three different kinds of CO on rhodium (gem-dicarbonyl, linear and bridged). The relative population of these CO species was found to depend on the adsorption temperature and support chemical composition.

(f) The higher activity and H_2-selectivity of Rh/$Ce_{0.15}Zr_{0.81}Mg_{0.05}O_2$ catalyst towards phenol steam reforming and water–gas shift reactions (lowest CO/CO_2 product ratio) is likely to be partly related to the higher surface concentration of Rh^{n+} cationic species present in the former catalyst compared to the 0.5% Rh/$Ce_{0.15}Zr_{0.85}O_2$ catalyst.

(g) The WGS reaction was found to take place effectively (X_{CO} > 80%) in the 350–500 °C range over all supported-Rh catalysts studied (Rh/$Ce_{0.15}Zr_{0.85}O_2$, Rh/$Ce_{0.15}Zr_{0.83}Mg_{0.02}O_2$ and Rh/$Ce_{0.14}Zr_{0.81}Mg_{0.05}O_2$). *In situ* DRIFTS–WGS reaction studies at 350 and 550 °C led to the identification of linear and bridged adsorbed CO on the Rh surface, and carbonates and formate (COOH) species on the support as reaction intermediate species. It was possible to see that the surface concentration of formates on the Rh/$Ce_{0.14}Zr_{0.81}Mg_{0.05}O_2$ is larger than that on the Rh/$Ce_{0.15}Zr_{0.85}O_2$ catalyst, likely explaining the higher WGS activity of the former compared to the latter catalyst, considering that formate could be seen as a potential active reaction intermediate species [39].

Acknowledgments

The financial support of the Cyprus Research Promotion Foundation (project PENEK/ENISX/0308/51) and of the Research Committee of the University of Cyprus is gratefully acknowledged. The authors also thank MEL Chemicals (UK) for providing the commercial catalyst support materials ($Ce_{0.15}Zr_{0.85}O_2$, $Ce_{0.15}Zr_{0.83}Mg_{0.02}O_2$ and $Ce_{0.14}Zr_{0.81}Mg_{0.05}O_2$).

References

[1] M. Ni, D.Y.C. Leung, M.K.H. Leung, K. Sumathy, Fuel Proc. Technol. 87 (2006) 461.
[2] W. McDowall, M. Eames, Energy Policy 34 (2006) 1236.
[3] C. Koroneos, A. Dompos, G. Roumbas, Chem. Eng. Proc. 47 (2008) 1261.
[4] G. Marbán, T. Valdés-Solís, Int. J. Chem. Res. Eng. 32 (2007) 1625.
[5] F. Orecchini, E. Bocci, Energy 32 (2007) 1006.
[6] D. Dayton, A Review of the Literature on the Catalytic Biomass Tar Destruction, NREL/TP-510-32815, National Renewable Energy Laboratory, USA, 2002.
[7] C. Franco, F. Pinto, I. Gulyurtlu, I. Gabrita, Fuel 82 (2003) 835.
[8] L. Shen, Y. Gao, J. Xiao, Biomass Bioenergy 32 (2) (2008) 120.
[9] T.A. Milne, N. Abatzoglou, R.J. Evans, Biomass Gasifier Tars: Their Nature, Formation and Conversion, NREL/TP-570-25357, National Renewable Energy Laboratory, USA, 1989.
[10] L. Devi, K.J. Ptasinski, F.J.J.G. Janssen, Biomass Bioenergy 24 (2003) 125.
[11] P.C.A. Bergman, S.V.B. van Paasen, H. Boerrigter, Pyrolysis and Gasification of Biomass and Waste, Expert Meeting, 30 Sept.–1 Oct., Strasbourg, France, 2002.
[12] R. Zhang, R. Brown, A. Suby, K. Cummer, Energy Convers. Manage. 45 (2004) 995.
[13] C.M. Kinoshita, Y. Wang, J. Zhou, J. Anal. Appl. Pyrolysis 29 (1994) 169.
[14] European Project, 6th FP, No. 5183309 (SES6), Biomass Fluidized Bed Gasification with In-Situ Hot Gas Cleaning, 2006–2009.
[15] J.N. Kuhn, Z. Zhao, L.G. Felix, U.S. Ozkan, Appl. Catal. B: Environ. 81 (2008) 14.
[16] H.A.M. Knoef, Handbook Biomass Gasification, BTG Biomass Technology Group BV, 2005, ISBN:90-810068r-r1-9.
[17] P.A. Simell, J.B. Bredenberg, Fuel 69 (1990) 1219.
[18] C.M. Kinoshita, Y. Wang, J.C. Zhou, Ind. Eng. Chem. Res. 34 (1995) 2949.

[19] W. Wang, N. Padban, Z. Ye, A. Andersson, I. Bjerle, Ind. Eng. Chem. Res. 38 (1999) 4175.
[20] D.L. Trimm, Catal. Today 49 (1999) 3.
[21] J.-S. Chang, D.-Y. Hong, X. Li, S.-E. Park, Catal. Today 115 (2006) 186.
[22] T. Horiuchi, K. Sakuma, T. Fukui, Y. Kubo, T. Osaki, T. Mori, Appl. Catal. A: Gen. 144 (1996) 111.
[23] K. Tomishige, T. Miyazawa, M. Asadullah, S. Ito, K. Kumimori, Green Chem. 5 (2003) 399.
[24] M. Asadullah, K. Tomishige, K. Fujimoto, Catal. Commun. 2 (2001) 63.
[25] M. Asadullah, T. Miyazawa, S. Ito, K. Kumimori, K. Tomishige, Energy Fuels 17 (2003) 842.
[26] M. Asadullah, S. Ito, K. Kumimori, M. Yamada, K. Tomishige, J. Catal. 208 (2002) 255.
[27] M. Asadullah, T. Miyazawa, S. Ito, K. Kumimori, M. Yamada, K. Tomishige, Appl. Catal. A: Gen. 255 (2003) 169.
[28] K. Tomishige, M. Asadullah, K. Kumimori, Catal. Today 89 (2004) 389.
[29] K. Polychronopoulou, J.L.G. Fierro, A.M. Efstathiou, J. Catal. 228 (2004) 417.
[30] K. Polychronopoulou, C.N. Costa, A.M. Efstathiou, Appl. Catal. A: Gen. 272 (2004) 37.
[31] C.N. Costa, T. Anastasiadou, A.M. Efstathiou, J. Catal. 194 (2000) 250.
[32] A.L. Patterson, Phys. Rev. 56 (1939) 978.
[33] P.S. Lambrou, C.N. Costa, S.Y. Christou, A.M. Efstathiou, Appl. Catal. B: Environ. 54 (2004) 237.
[34] C.N. Costa, S.Y. Christou, G. Georgiou, A.M. Efstathiou, J. Catal. 219 (2003) 259.
[35] D.A. Constantinou, A.M. Efstathiou, Catal. Today 143 (2009) 17.
[36] D.A. Constantinou, J.L.G. Fierro, A.M. Efstathiou, Appl. Catal. B: Environ. 90 (2009) 347.
[37] B.C. Smith, Fundamentals of Fourier Transform Infrared Spectroscopy, CRC Press, 1996.
[38] F.M. Hoffmann, Surf. Sci. Rep. 3 (1983) 107.
[39] G.G. Olympiou, C.M. Kalamaras, C.D. Zeinalipour-Yazdi, A.M. Efstathiou, Catal. Today 127 (2007) 304, and references therein.
[40] C.M. Kalamaras, P. Panagiotopoulou, D.I. Kondarides, A.M. Efstathiou, J. Catal. 264 (2009) 117, and references therein.
[41] X. Wang, G. Lu, Y. Guo, Y. Xue, L. Jiang, Y. Guo, Z. Zhang, Catal. Today 126 (2007) 412.
[42] M.Y. Youn, J.G. Seo, K.M. Cho, S. Park, D.R. Park, J.C. Jung, I.K. Song, Int. J. Hydrogen Energy 33 (2008) 5052.
[43] M. Yashima, K. Morimoto, N. Ishizawa, M. Yoshimura, J. Am. Ceram. Soc. 76 (7) (1993) 1745.
[44] C. Janvier, M. Pijolat, F. Valdivieso, M. Soustelle, C. Zing, J. Eur. Ceram. Soc. 18 (1998) 1331.
[45] B. Yue, R. Zhou, Y. Wang, X. Zheng, J. Mol. Catal. 238 (2005) 241.
[46] J.R. Anderson, K.C. Pratt, Introduction to Characterization and Testing of Catalysts, Academic Press, New York, 1985.
[47] Y. Nagai, T. Hirabayashi, K. Dohmae, N. Takagi, T. Minami, H. Shinjoh, S. Matsumoto, J. Catal. 242 (2006) 103.
[48] M. Boaro, M. Vicario, C. de Leitenburg, G. Dolcetti, A. Trovarelli, Catal. Today 77 (2003) 407.
[49] C. de Leitenburg, A. Trovarelli, J. Kaŝpar, J. Catal. 166 (1997) 98.
[50] G.R. Rao, P. Fornasiero, R.D. Monte, J. Kaŝpar, G. Vlaic, G. Balducci, S. Meriani, G. Gubitosa, M. Graziani, J. Catal. 162 (1996) 1.
[51] P. Fornasiero, R.D. Monte, G.R. Rao, J. Kaŝpar, S. Meriani, A. Trovarelli, M. Graziani, J. Catal. 151 (1995) 168.
[52] Y. Li, D. He, Q. Zhu, X. Zhang, B. Xu, J. Catal. 221 (2004) 584.
[53] W. Khaodee, B. Jongsomjit, S. Assabumrungrat, P. Praserthdam, S. Godo, Catal. Commun. 8 (2007) 548.
[54] M. Daturi, C. Binet, J.C. Lavalley, G. Blanchard, Surf. Interface Anal. 30 (2000) 273.
[55] F. Gaillard, Catal. Lett. 95 (2004) 23.
[56] E. Florez, P. Fuentealba, F. Mondragón, Catal. Today 133/135 (2008) 216.
[57] C. Binet, M. Daturi, J.-C. Lavalley, Catal. Today 50 (1999) 207.
[58] T. Szailer, É. Novák, A. Oszkó, A. Erdohelyi, Top. Catal. 46 (2007) 79.
[59] A. Trovarelli, C. De Letenburg, G. Dolcetti, J. LLorca, J. Catal. 151 (1995) 111.
[60] G. Busca, V. Lorenzelli, Mater. Chem. 7 (1982) 89.
[61] Z. Hou, T. Yashima, Catal. Lett. 89 (2003) 193.
[62] J. Gamman, G.J. Millar, G. Rose, J. Dreman, J. Chem. Soc., Faraday Trans. 94 (1998) 701.
[63] T. Jin, Y. Zhou, G.J. Mains, J.M. White, J. Phys. Chem. 91 (1987) 5931.
[64] R.W. McCabe, L.D. Schmidt, Surf. Sci. 60 (1976) 85.
[65] T. Arakawa, K. Takada, Y. Tsunemine, Mater. Res. Bull. 24 (1989) 395.
[66] T. Ioannides, X. Verykios, J. Catal. 140 (1993) 353.
[67] A.M. Efstathiou, J. Mol. Catal. 69 (1991) 41.
[68] V.A. Tsipouriari, A.M. Efstathiou, X.E. Verykios, J. Catal. 161 (1996) 31.
[69] L.G. Tejuca, A.T. Bell, J.L.G. Fierro, M.A. Peña, Appl. Surf. Sci. 31 (1988) 301.
[70] L.H. Dubois, G.A. Somorjai, Surf. Sci. 91 (1980) 514.
[71] F. Frusteri, S. Freni, L. Spadaro, V. Chiodo, G. Bonura, S. Donato, S. Cavallaro, Catal. Commun. 5 (2004) 611.
[72] D. Duprez, P. Pereira, A. Miloudi, R. Maurel, J. Catal. 75 (1982) 151.
[73] K. Polychronopoulou, A.M. Efstathiou, Catal. Today 112 (2006) 89.
[74] L. Garcia, R. French, S. Czernik, E. Chornet, Appl. Catal. A: Gen. 201 (2000) 225.
[75] C. Rioche, S. Kulkarni, F.C. Meunier, J.P. Breen, R. Burch, Appl. Catal. B: Environ. 61 (2005) 130.
[76] C. Diagne, H. Idriss, K. Pearson, M.A. Gómez-García, A. Kiennemann, C. R. Chimie 7 (2004) 617.
[77] C. Diagne, H. Idriss, A. Kiennemann, Catal. Commun. 3 (2002) 565.
[78] F. Frusteri, S. Freni, V. Chiodo, L. Spadaro, O.D. Blasi, G. Bonura, S. Gavallaro, Appl. Catal. A: Gen. 270 (2004) 1.
[79] Y. Choi, H.G. Stenger, J. Power Sources 124 (2003) 432.
[80] D.I. Kondarides, T. Chafik, X.E. Verykios, J. Catal. 191 (2000) 147.
[81] C.A. Rice, S.D. Worley, C.W. Curtis, J.A. Guin, A.R. Tarrer, J. Chem. Phys. 74 (1981) 6487.
[82] A.C. Yang, C.W. Garland, J. Phys. Chem. 61 (1957) 1504.
[83] Y.T. Yates Jr., T.M. Duncan, S.D. Worley, R.W. Vaughan, J. Chem. Phys. 70 (1979) 1219.
[84] S. Trautmann, M. Baerns, J. Catal. 150 (1994) 335.
[85] Z.L. Zhang, A. Kladi, X.E. Verykios, J. Mol. Catal. 89 (1994) 229.
[86] M. Haneda, K. Shinoda, A. Nagane, O. Houshito, H. Takagi, Y. Nakahara, K. Hiroe, T. Fujitani, H. Hamada, J. Catal. 259 (2008) 223.
[87] T. Básági, T.S. Zakar, F. Solymosi, Appl. Catal. B: Environ. 66 (2006) 147.
[88] D.I. Kondarides, Z. Zhang, X.E. Verykios, J. Catal. 176 (1998) 536.
[89] C. Larese, M.L. Granados, F.C. Calisteo, R. Mariscal, J.L.G. Fierro, Appl. Catal. B: Environ. 62 (2006) 132.
[90] C. Force, J.P. Belzunequi, J. Sanz, A.M. Arias, J. Soria, J. Catal. 197 (2001) 192.
[91] J.N. van Vegten, D. Ferri, M. Maciejewski, F. Krumeich, A. Baiker, J. Catal. 249 (2007) 269.
[92] H.C. Yao, W.G. Rothschild, J. Chem. Phys. 68 (11) (1978) 4774.
[93] P. Basu, D. Panayotov, J.T. Yates Jr., J. Am. Chem. Soc. 110 (1988) 2074.
[94] T. Shido, Y. Iwasawa, J. Catal. 136 (1992) 493.
[95] Y. Denkwitz, A. Karpenko, V. Plzak, R. Leppelt, B. Schumacher, R.J. Behm, J. Catal. 246 (2007) 74.
[96] G. Busca, J. Lamotte, J.-C. Lavalley, V. Lorenzelli, J. Am. Chem. Soc. 109 (1987) 5197, and references therein.